This is a preprint, the final version is subject to change, of the American Mineralogist (MSA)
Cite as Authors (Year) Title. American Mineralogist, in press.
DOI: https://doi.org/10.2138/am-2020-7010

Revision 2

A new emerald occurrence from Kruta Balka, Western Peri-Azovian region, Ukraine: Implications for understanding the crystal chemistry of emerald

GERHARD FRANZ[1], OLEKSII VYSHNEVSKYI[2], MICHAIL TARAN[2], VLADIMIR KHOMENKO[2], MICHAEL WIEDENBECK[3], FERRY SCHIPERSKI[1], JÖRG NISSEN[4]

[1]Institute for Applied Geosciences, Technical University Berlin, D-10587 Berlin, Germany
[2]The National Academy of Sciences of Ukraine, M. P. Semenenko Institute of Geochemistry, Mineralogy and Ore Formation, 34, Palladina av., Kyiv, 03142, Ukraine
[3]GFZ German Research Centre for Geosciences, Telegrafenberg, D-14473 Potsdam, Germany
[4]ZE Electron microscopy, Technical University Berlin, D-10623 Berlin, Germany

ABSTRACT

We investigated emerald, the bright-green gem varietal of beryl, from a new locality at Kruta Balka, Ukraine and compare its chemical characteristics with those of emerald from selected occurrences worldwide (Austria, Australia, Colombia, South Africa, Russia) in order to clarify the types and amounts of substitutions as well as the factors controlling such substitutions. On selected crystals Be and Li were determined by secondary ion mass spectrometry, which showed that the generally assumed value of 3 Be atoms per formula unit (apfu) is valid; only some examples such as emerald from Kruta Balka deviate from this (resulting in 2.944 Be apfu). An important substitution in emerald (expressed as exchange vector with the additive component $Al_2Be_3Si_6O_{18}$) is $(Mg,Fe^{2+})NaAl_{-1}\square_{-1}$, leading to a hypothetical end-member $NaAl(Mg,Fe^{2+})[Be_3Si_6O_{18}]$ called femag-beryl with Na occupying a vacancy position (□) in the structural channels of beryl. Based on both our results and data from the literature, emeralds worldwide can be characterized based on the amount of femag-substitution. Other minor substitutions in Li-bearing emerald include the exchange vectors $LiNa_2Al_{-1}\square_{-2}$ and $LiNaBe_{-1}\square_{-1}$, where the former is unique to the Kruta Balka emeralds. Rarely, some Li can also be situated at a channel site, based on stoichiometric considerations. Both Cr- and V-distribution can be very heterogeneous in individual crystals, as shown for material from Kruta Balka, Madagascar and Zambia, but taking average values available for emerald occurrences, the Cr/(Cr+V) ratio (Cr#) in combination with the Mg/(Mg+Fe) ratio (Mg#) and the amount of femag-substitution allows emerald occurrences to be characterized. The 'ultramafic' schist-type emeralds with high Cr# and Mg# come from occurrences where the Fe-Mg-

Cr-V component is controlled by the presence of ultramafic meta-igneous rocks. Emeralds with highly variable Mg# come from 'sedimentary' localities, where the Fe-Mg-Cr-V component is controlled by metamorphosed sediments such as black shales and carbonates. A 'transitional' group has both metasediments and ultramafic rocks as country rocks. Most 'ultramafic' schist type occurrences are characterized by a high amount of femag-component, whereas those from the 'sedimentary' and 'transitional' groups have low femag content. Growth conditions derived from the zoning pattern - combined replacement, sector and oscillatory zoning - in the Kruta Balka emeralds indicate disequilibrium growth from a fluid along with late-stage Na-infiltration. Inclusions in Kruta Balka emeralds (zircon with up to 11 wt% Hf, tourmaline, albite, Sc-bearing apatite) point to a pegmatitic origin.

Keywords: beryl, substitution mechanisms, ion microprobe analysis, electron microprobe analysis, optical spectroscopy, infrared spectroscopy, Kruta Balka, Ukraine

INTRODUCTION

Beryl, ideally $Al_2Be_3[Si_6O_{18}]$, is the most abundant Be-mineral; solid solution between beryl and other components has been the subject of several earlier investigations (e.g. reviews by Černý 2002; Hawthorne and Huminicki 2002). The crystal chemistry of emerald, its green gem varietal of beryl, has also been studied extensively (e.g. Groat et al. 2008; Marshall et al. 2012; Loughrey et al. 2013; Hewton et al. 2013; Aurisicchio et al. 2018). The structure of this cyclosilicate (space group *P6/mcc*; Gibbs et al. 1968) consists of Si_6O_{18}-rings lying in planes parallel to (0001), connected by Be-tetrahedra and Al-octahedra. Stacking of the rings creates channels with two additional positions (□), a large one (0,0,1/4; 2a) above the center of the rings, a smaller one (0,0,0; 2b) at the level of the rings.

A number of substitutions are known to be important in emerald (Table 1). Taking $^{ch}\square\,^{vi}Al_2\,^{iv}Be_3[^{iv}Si_6O_{18}]$ as the additive component, the simple exchange vector $Fe^{3+}Al_{-1}$ creates the Fe^{3+}-end-member stoppaniite, $ScAl_{-1}$ leads to the Sc-analogue bazzite, and $Cr^{3+}Al_{-1}$ and $V^{3+}Al_{-1}$ are responsible for the emerald color (end-members are not known). The vacancy positions can be occupied by H_2O as a function of *P* and *T* (Pankrath and Langer 2002), but also with large cations such as Na^+ (at 2b) and Cs^+ (at 2a), allowing for charge balance of coupled substitutions on the tetrahedral (Be) and octahedral (Al) sites. The coupled exchange vector $LiCsBe_{-1}\square_{-1}$ creates pezzottaite $CsAl_2Be_2Li[Si_6O_{18}]$ ('tetrahedrally substituted beryl'; Aurisicchio et al. 1988). Its Na-analog avdeevite $(Na,Cs)(Be_2Li)Al_2[Si_6O_{18}]$ was found by Agakhanov et al. (2019). In many beryls, especially in emerald, there is an important substitution $(Mg,Fe^{2+})NaAl_{-1}\square_{-1}$, leading to a hypothetical end-member $NaAl(Mg,Fe^{2+})Be_3[Si_6O_{18}]$ called 'femag-beryl' (Schaller et al. 1962).

Lithium can also be incorporated via $LiNa_2Al_{-1}\square_{-2}$, (Beus 1966; 'octahedrally substituted beryl'; Aurisicchio et al. 1988). The high-temperature polymorph of cordierite, indialite, is isostructural with beryl, though it does not show significant solid solution with beryl. However, synthetic Be-cordierite $Mg_2[Al_2BeSi_6O_{18}]$ (Hölscher and Schreyer 1986) is a possible candidate for an additional substitution involving tetrahedral and octahedral sites, $^{iv}Al_2{}^{vi}Mg_2{}^{vi}Al_{-2}{}^{iv}Be_{-2}$, simplified to $MgBe_{-1}$.

In recent years the number of known emerald occurrences has grown as well as increasing levels of research into emerald's formation conditions (e.g. Groat et al. 2002; Hewton et al. 2013; Loughrey et al. 2013; Marshall et al. 2004, 2012, 2017; Pignatelli et al. 2015; Renfro et al. 2017). With regards to emerald's crystal chemistry, a well-established data base of electron microprobe analyses (EPMA) already exists (see references above). EPMA, however, can only provide partial analyses, because Be as the major and characteristic element, and Li as an important minor element cannot be determined, which introduces uncertainty in the formula calculation. Only recently Aurisicchio et al. (2018) presented a data set including Be and Li determinations by secondary ion mass spectrometry (SIMS). In addition, the unknown ratio Fe^{3+}/Fe^{2+} as well as unknown water contents make a straight-forward formula calculation impossible.

We describe emerald from Kruta Balka in the Archean-Paleoproterozoic part of the eastern block of the Ukrainian Shield, a new occurrence first reported by Taran et al. (2005), where the exceptional Li substitution is $LiNa_2Al_{-1}\square_{-2}$. This Ukrainian locality is related to pegmatites at the contact to both meta(ultra)mafic rocks and metapelites, and the emeralds are characterized by both of the coloring elements Cr and V. Growth conditions of these emeralds, derived from the zoning patterns and the observed mineral inclusions, indicate a pegmatitic origin.

In addition, we determined Be and Li contents of beryl from several emerald occurrences by SIMS and, together with EPMA data, determined the cation assignment with constraints on substitution mechanisms in emerald. We show that for most emeralds the assumption of 3.000 Be atoms per formula unit (apfu) is valid and confirm that in addition to the substitutions $Cr^{3+}Al_{-1}$, $V^{3+}Al_{-1}$, $Fe^{3+}Al_{-1}$, and $(Mg,Fe^{2+})NaAl_{-1}\square_{-1}$, minor Li is incorporated not only via $LiNaBe_{-1}\square_{-1}$, but also via $LiNa_2Al_{-1}\square_{-2}$, albite rarely. In a few cases, Li occupies a channel position. In some emeralds there may be an additional substitution with the Be-cordierite component $MgBe_{-1}$ (Hölscher and Schreyer, 1986). Compilation of emerald analysis of known occurrences worldwide leads to the conclusions that on the basis of the amount of femag substitution, Mg/(Mg+Fe) (= Mg#), and their Cr/(Cr+V) (= Cr#) ratios, the critical element concentrations Mg, Fe, Cr, and V are controlled by ultramafic country rocks at some localities, which are distinct from occurrences where (meta)sedimentary rocks provide the source of Mg, Fe, Cr, and V. At some localities (transitional), such as Kruta Balka, both types of country rocks are present.

SAMPLES AND ANALYTICAL METHODS

SIMS analysis

Thick sections of emerald samples (Habachtal, Austria; Ural Mts., Russia; Muzo, Columbia; Leyendorp, South Africa; Western Australia; Table EA 1) were prepared from the same seven crystals from which thin sections were cut for EPMA. We used the Cameca ims 6f SIMS instrument at GFZ-Potsdam to quantify Li and Be concentrations at a spatial resolution of *circa* 5 µm. The actual analyses employed a nominally 12.5 kV, mass filtered $^{16}O^-$ primary beam operated at 1 nA current. In order to suppress surface related contaminants, which is necessary for the quantification of Li at low and trace concentrations, we conducted a 5 min pre-burn using a 25 x 25 µm raster over each analysis location. This was followed by an unrastered 3 min pre-burn used to establish equilibrium sputtering conditions.

Secondary ions were extracted with a 10 kV acceleration potential. The mass spectrometer was operated at a mass resolving power of $M/\Delta M = 3500$ which is more than adequate for eliminating all significant isobaric interferences. A 750 µm diameter field aperture, equivalent to a 60 µm diameter field-of-view at the sample surface, was used in conjunction with a 50 eV energy bandpass using no energy off-set. Our method provided a count rate of around 300 kHz on the ^{28}Si mass station. A single analysis consisted of 5 blocks of 5 cycles each of the peak stepping sequence: 6.9 Da (0.1 s per cycle; needed for the pre-burn), ^{7}Li (2 s), ^{9}Be (2 s), ^{27}Al (2 s) and ^{28}Si (2 s). Thus a single analysis required *circa* 8 min including the automatic 3 min pre-burn. We assessed whether the use of ^{27}Al or ^{28}Si provided the better quality data. Based on the observed repeatability of the results from our reference materials it was concluded that the use of ^{28}Si for normalization was more robust, and hence we did not make use of the acquired ^{27}Al data.

One of the largest challenges for our SIMS analyses was the identification and characterization of suitable reference materials. In total six samples of beryl, both natural and synthetic in origin, were tested by SIMS for having homogeneous Li and Be distributions. From these results we selected three of these materials based both on their apparent homogeneities and their spread in Li and Be contents. These three samples were then analyzed for their Li and Be contents by solution ICP-MS analyses (Table EA 2). The Si contents of these samples, required for the normalization procedure, were based on earlier EPMA data collected from different fragments of the same crystals. Based on 28 SIMS analyses of the reference materials we estimate our repeatability for Be determinations to be *circa* 1% (rel.) and the repeatability for Li to be *circa* ±2% at high concentrations and *circa* ±8% at low Li abundances (1 sd). Based on an intercomparison of the three reference materials using the average divergence of the 28 reference material measurements from the calibration line calculated from the ICP-MS results, we estimate the trueness of our method for Be to be 0.5%. Using the same approach applied only to the two Li-rich reference

samples, we estimate our trueness for Li results to be 2.6%. In the case of the Li-poor synthetic reference beryl the SIMS quantification yielded systematically low concentration values by a factor of 65%. This suggests that Li blank and/or blank correction issues may be affecting the SIMS and/or ICP-MS data at sub-10 $\mu g\ g^{-1}$ level. Any such effect would have only a negligible impact on the Li concentrations, which we determined by SIMS in our "unknown" samples. The concentrations of Be and Li in these unknowns are compiled in Table 2.

EPMA and colorimetry analysis

The JEOL JXA-8530F field emission microprobe at TU Berlin was used to investigate the same crystals that were studied with the SIMS method. EPMA data were acquired using a 15 kV, 20 nA beam with a defocused 15 μm probe diameter and our calibration was based on Astimex mineral reference materials (olivine for Mg, hematite for Fe, rutile for Ti, andalusite for Si and Al, albite for Na) and pure metal (Cr, Mn, V,). Matrix corrections of WDS analyses were done in ZAF mode. Peak counting times were 20 s and counting times for background 10 s on each side of the peak. For other emeralds we used a focused beam of 2 μm. The relative counting uncertainties of X-ray intensities were 0.26% for Si, 0.51% for Al, 4.36% for Fe, 11.07% for Cu, 17.33% for Cr and 26.86% for Ni. Lithium contents for selected crystals from this data set were determined at the University of Kiel, Germany from $HF/HClO_2$ digestion in teflon autoclave at 150 °C with ~20 mg hand-picked, high-purity emerald using atomic absorption spectroscopy (data listed in Table EA1). H_2O contents were measured by colorimetry (Karl-Fischer method; at University of Bochum) with an Alimex, model CA-02 instrument, for which the relative standard deviation is estimated as ± 3% (data listed in Table EA1). Analytical details of EPMA for some samples, including a pegmatitic, relatively pure beryl from Namibia, were used to check the reliability of the EPMA and the formula calculation procedure, are given in Franz et al. (1986).

Three samples of Kruta Balka beryl (localities for KB #16 and #18 see Figs. 1, 2; sample KBE is from the same area, but its exact sampling location has not been provided) were studied by both EPMA and spectroscopy. Two additional single crystals KB-1 and KB-2 were selected for mapping of element distribution in the wave-length dispersive mode of the JEOL microprobe at TU Berlin. An additional small emerald sample was used for X-ray diffraction (XRD).

The chemical compositions of KB #16 and #18 and of the inclusions were determined using C-coated samples with a field-emission scanning electron microscope JSM-6700F equipped with an energy-dispersive spectrometer JED-2300 (JEOL) at IGMOF NAS of Ukraine (Kyiv) at operating conditions of 20 kV accelerating voltage, 1.0 nA beam current, 1 μm beam size, and a counting time of 60 s. Pure Si, Ti, Zr, Hf, Al, Cr, V, Fe, Mn and synthetic MgO, CaF_2, Na_3AlF_6, KCl were used for calibration. Raw counts were corrected for matrix effects with the ZAF algorithm implemented by JEOL. The sample KB #18 was also analyzed at IGMOF NAS of Ukraine (Kyiv)

using a JEOL JCXA-733 electron microprobe, equipped with three vertical wavelength dispersive spectrometers (analytical conditions: accelerating voltage of 15 kV, beam current 20 nA, beam diameter of 2 μm, peak counting times of 30 s, for background 10 s on each side of the peak, routine ZAF correction). Reference materials were pure metals Ti, Cr, V, Fe, Mn, natural quartz and albite, and synthetic compounds MgO, CaF_2, KCl. The KBE sample was investigated at TU Berlin. Some of the data on crystals KB#16 and KB#18 and of inclusions were already presented in Taran et al. (2005).

Optical Spectra

Optical absorption and diffuse reflectance spectra between 350-2500 nm and 350-1000 nm, respectively, were measured with a single-beam spectrophotometer consisting of a SpectraPro-275 grating monochromator at the Academy of Sciences, Kiev, combined with a polarized mineralogical microscope MIN-8. The diameter of the measuring light spot was ≤ 0.5 mm. A description of the spectrophotometer and procedure used for registration of absorption and reflectance spectra can be found in e.g. Taran and Langer (2001) and Taran et al. (2004). The refractive indices for each of the two samples #16 and #18 yielded values of n_ω = 1.588-1.590, n_ε = 1.580-1.582, $\Delta n = 0.008 \pm 0.002$ (Taran et al. 2005). The slight variations of the values within each sample are due to their chemical heterogeneity and this level of variation is similar to that found for other deposits worldwide (Anderson 1990; Feklichev 1964; Gavrilenko 1998; Gromov 1990; Tretyakova and Benavides 1987). The specific gravity was determined by hydrostatic weighing as 2.70-2.72 g cm^{-3} (Taran et al. 2004), which is slightly lower than that from emeralds of most other deposits, for which the specific gravity is usually 2.72-2.75 g cm^{-3}, probably caused by their relatively low Fe contents.

Polarized infrared spectra

Polarized infrared absorption spectra of the KBE sample were measured at room temperature in the spectral range 6000 - 1500 cm^{-1} by means of a Bruker FTIR spectrometer IFS 66 equipped with an IR-microscope at TU Berlin. Spectra were scanned with a measuring spot of 60 μm diameter and at a spectral resolution of 2 cm^{-1}. The time-averaged signal was collected over 200 scans. The reference spectra were measured in air. Curve fitting of overlapping absorption bands was performed with the program PeakFit. For the FTIR transmission measurements, fragments of the KBE beryl crystal were cut along **c** axis, ground down to thickness of 55 μm and polished on both sides.

X-ray diffraction

XRD was conducted on a D2 Phaser (Bruker, Germany) at TU Berlin. The sample was ground in a corundum mortar for several minutes and placed on a Si-single crystal sample holder. Measurement parameters were set to a 2θ stepsize of 0.01° in the range of 5-85°2θ with 5 s per step.

The Rietveld method was applied to the observed data using the crystallography data analysis software GSAS-II (Version 3816). Structural data from Evdokimova et al. (1989) were used as initial phase.

Refined parameters were applied in following sequence: background (Chebyschev model using 7 coefficients), zero offset, sample displacement, lattice constants, crystallite size, atom position and thermal motion (refined in the listed order). The latter two were only refined for Si and Al. Data of crystal chemistry from microprobe analyses was implemented in the model. Limits of the refinement were set from 10 to 80° 2θ to avoid high background signals from the initial part of the diffractogram. Corresponding atomic site fractions are listed in Table EA 5.

Compilation of literature data set

To compare the new data from Kruta Balka with emeralds worldwide, we compiled a data base of EPMA results from the literature, including our new data for several localities, and present an average composition for each locality; for analyses and references see below. For this data base all analyses were calculated on the basis of 18 O and 3.000 apfu Be, irrespective if BeO determinations were available, thereby achieving a comparable data set. As it will be shown in the Discussion, the assumption of 3.000 apfu Be introduces only a minor uncertainty for the other cations. All Fe was calculated as Fe^{2+}, although it is known that some of Fe_{tot} is trivalent, because Fe^{3+}/Fe^{2+} data are extremely scarce.

This data set contains all localities known to us, including new analyses for a sample from Namibia, which are not yet published, and unpublished data for Ethiopia, Davdar (China), and McKenzie Mts. (Canada) (Marshall, pers. comm.). It should be noted that such a data set is necessarily heterogeneous, because the number of spot analyses, measured elements and methods, number of samples, and purpose of sampling (gemological vs. petrological or crystal chemistry) differ among the studies. The reader should be aware that these are *typical* compositions, and these data must be used with caution for provenance fingerprinting. For comparison with individual data the reader is referred to the literature about a specific deposit and to the study of Aurisicchio et al. (2018), who also gave trace element contents of emerald samples from several occurrences. A statistically significant study would require a large number of samples from one locality, e.g. Kochelek et al. (2015) studied between 10 and 30 samples from each locality for a provenance analysis of ruby and sapphire; such a large number of samples is available from only a few of the known emerald localities.

RESULTS

Kruta Balka emeralds

Geological setting. Bright green emerald-like beryl in Ukraine was first found in 1964-1967 during exploration for rare-metal pegmatites of the Kruta Balka area (Fig. 1) in the Western Peri-Azovian region, where Archean and Early Proterozoic metamorphic complexes with metamorphosed alkali intrusions and pegmatites are widespread. The rare-metal pegmatite occurrence of Kruta Balka, carrying significant contents of Be, Ta, Li, and Cs, is located in the valley of the Berda River, 31 km north of Berdyansk. Its detailed geological characteristics are presented in Chornokur and Yaskevych (2010) and Shatalov (2017). The pegmatites are localized at the boundaries of the Precambrian Sorokin greenstone belt (also named as Sorokinskaya graben-syncline), which is in the western part of the Pryazovskyi domain of the Ukrainian Shield (Fig. 1). This domain is interpreted as a deep linear zone of rifting in the Archaean granulite-facies gneissic basement, visible today as a narrow band of supracrustal formations 35-40 km in length and with a width of up to 2 km. It is bordered by sub-parallel deep faults. The level of erosion within its boundaries can reach 5 km, hence only its deeper parts have been preserved.

The rocks at Kruta Balka are Archean granodiorites, metabasites (amphibolites, pyroxenites), meta-ultrabasites (dunites etc.) and clastic metasediments of the Osipenkovo suite (Fig. 2a). The thickness of metabasites and meta-ultrabasites ranges from a few meters up to 300 m, and their length along strike can reach several km. The metasediments are dominantly metapelites (different types of micaschists with garnet, biotite, muscovite, staurolite, tourmaline). Metapsammites, metaconglomerates, biotite-, amphibole- and feldspathic quartzites, and calcareous rocks are present in minor amounts.

Pegmatite veins and bodies are present with thicknesses from 0.5 m to several tens of meters (Fig. 2b). They mainly consist of elongated bodies with plate-like or mushroom-like geometries with an aspect ratio of 6:1 or more, and a variable morphology, depending on the rheological properties of the host rocks; in granitoids such veins have consistent forms. The width of the pegmatites gradually decreases as one approaches the metamorphic host rocks. The thickness of those veins nearest to the mafic and ultramafic rocks sharply increases, forming numerous branched apophyses. Where pegmatite veins penetrate into metasediments, they quickly bifurcate and wedge out.

Pegmatites vary in composition as a function of their vertical position. Thin, mainly microcline-bearing veins dominate in the lower part, whereas quartz-albite and albite-spodumene-rich veins dominate in the upper part. The largest bodies near to the surface, partially exposed at the erosion level, are quartz-albite pegmatites with quartz cores. Accessory minerals include tourmaline, garnet, magnetite, apatite, beryl, tantalite, columbite, chrysoberyl, eschinite, spodumene, and petalite. The K-Ar age of muscovite from the pegmatites is 2240 (+72/-14) Ma (Rozanov and Lavrinenko 1979).

Emerald is found in the extensions of grey muscovite-biotite veins near their contacts with the country rocks (Fig. 3). Mica-rich veins with emerald are typically up to 3-4 cm thick and are included in a pegmatitic rock composed predominantly of albite and, to a lesser extent, grey quartz. Such veins usually start from the contact and can penetrate into the pegmatite to a depth of 2 m. Drill cores showed that to a depth of 50-70 m the pegmatitic veins are relatively rare, but below this level they can constitute up to half the volume of the rock.

Emerald crystals of predominantly hexagonal-prismatic habit with a poorly developed prism $(10\bar{1}1)$ and a well-developed pinacoid (0001) form aggregates or individual, non-orientated crystals, typically 5-20 mm in length and 3-15 mm in diameter, which are intimately intergrown with both greenish (Cr-bearing) and colorless muscovite (Fig. 4). The faces $(11\bar{2}1)$ are rare. The color distribution is generally patchy.

Chemical composition. The average chemical compositions of the Kruta Balka (KB) samples are given in Table 3 (individual data points see Table EA 4a), including Li-determinations by flame photometry (Rozanov and Lavrinenko 1979), with an average value of 0.41 wt% Li_2O. Formula calculations assuming 3.000 Be apfu yield calculated BeO contents between 13.45 to 13.73 wt%.

Specific features of the KB emeralds are their low MgO and FeO contents, which do not exceed 1.0 wt%, and a high Na_2O content of ~1.8 wt%. The average concentrations of Cr and V are 0.015 apfu and ~0.004 apfu, respectively, but there is a distinct chemical heterogeneity, which mimics the patchy optical color distribution, reaching up to 0.012 apfu V (equivalent to 0.20 wt% V_2O_3). As an example to highlight the general heterogeneity of KB emeralds, the data are compared to Cr-V data (Fig. 5) from the Sandawana, Zambia (Zwaan et al. 1997) and the Mananjary, Madagascar (Table EA 1) localities, which show similar heterogeneities in Cr contents.

The two crystals KB-1 and KB-2, selected for mapping of the element distribution, show different types of growth zoning. The central part of KB-1 (Fig. 6), which has abundant inclusions, shows replacement structures of former euhedral crystals, with Cr-Mg-poor dark areas (see center of Cr- and Mg-images). All four elements Mg, Fe, Cr, and V are correlated, though hardly visible in the images because of low concentrations; Al and Mg are inversely correlated. Cr is also enriched in biotite, in late stage chlorite, and in muscovite intergrowths with biotite, whereas large muscovite inclusions in emeralds are generally Cr-poor. Contrary to Cr, V is slightly concentrated in apatite. Towards the rim of the emerald crystal, the Cr distribution is oscillatory. The Na distribution in KB emeralds does not correlate with the trends seen for other element concentrations; Na is enriched in an irregular network of µm-wide veins where some veins are oriented subparallel and -perpendicular to *c*. Scandium, a trace element often observed in beryl, is enriched in apatite, but not in KB emeralds. The

concentrations of Sc in general correlate with Cr, Mg, and V distributions.

Element mapping of the inclusion-free crystal KB-2 (Fig. 7) does not show replacement structures, but rather a combination of sector and oscillatory zoning. The growth zones are parallel to the prism faces, the basal pinakoid (0001) and pyramids $(11\bar{2}2)$, and are obvious in alternation of Cr-rich and Cr-poor zones. In these zones Al and Cr are anti-correlated; likewise, Mg and Sc (and Fe; hardly visible in the image because of low concentration) are anti-correlated. The zigzag pattern of Mg distribution in the internal part of the crystal indicates sector zoning (see dashed lines in Mg-image) with the **c**-sector enriched in Mg whereas the **a**-sector is enriched in Sc. Traces of sectors follow the growth direction, overprinted by zones without sectors, indicating several growth pulses. The outer part of the crystal is oscillatory zoned, well visible in Cr parallel to the prism faces, but also in Al, Mg, and Sc oscillation. In these outer parts of the crystal Cr is preferentially enriched in planes perpendicular to the **c**-axis. In the exterior part of this crystal Na is positively correlated with Mg, but also enriched in narrow areas along cracks oriented subparallel and -perpendicular to the crystal's **c**-axis.

XRD. Next to beryl, muscovite, quartz and corundum (impurity from the corundum mortar) were identified in minor amounts (<1 wt%). Unit cell parameters were determined to a = 9.219±0.014, c = 9.208±0.007 and V = 677.8±1.7 (uncertainty given as 6σ; details of site fractions in Table EA 5). The Rietveld model was found to be insensitive to changes in fractions of Li and Be at the tetrahedral position (x = 0.5; y = 0.0; z = 0.25). Even a complete substitution of Be by Li, with constant fractions of all other elements, did not change the model significantly.

Inclusions. Most of the solid inclusions (identified by EDS analyses; Table EA 4b-f) in KB emeralds (Fig. 8) are muscovite, dravite-shorl as numerous almost black, elongated prismatic crystals, and minor albite (≤ 0.01 mol% K-feldspar and anorthite each) and biotite. Chlorite and an unidentified Al-rich sheet silicate that are in parallel growth with muscovite occur along cracks and at the margins of muscovite inclusions. Calculation of the Li_2O content of the tourmaline inclusions from EPMA (normalized to 31 O and 4 OH) yielded 0.39 wt% Li_2O, corresponding to 0.259 apfu Li, which is close to the value determined for beryl from Kruta Balka. The amount of vacancy positions in the tourmaline is ~0.2 apfu, its Mg# is ~0.5 (Table EA 4c). Euhedral zircon crystals 10 to 30 µm in size have up to 11 wt% HfO_2 (Table EA 4e). Apatite crystals with a remarkable enrichment of Sc (~0.7 wt% Sc_2O_3) were also observed (Table EA 4f).

Spectroscopy. The optical absorption and diffuse reflectance spectra of KB emeralds (Fig. 9) confirm the isomorphic substitution of Al by Cr. In the visible range (~380-750 nm) of the absorption spectrum of sample #18 (Fig. 9a) there are distinct characteristic bands and lines, caused by electronic dd-transitions of Cr^{3+}-ions. The two broad and intense absorption bands with maxima at 410-440 nm and 600-640 nm are caused by electron spin-allowed transition ${}^4A_{2g} \rightarrow {}^4T_{2g}$ and ${}^4A_{2g}$

$\rightarrow {}^4T_{1g}$ of $^{[vi]}Cr^{3+}$, respectively (Wood and Nassau, 1968). The splitting of the bands into two components differing by energy and polarization is due to a reduction in symmetry of the structural position of Cr^{3+} from O_h to D_3 (Platonov et al.1979), which is also found in the absorption spectra of synthetic emeralds (e.g. Taran and Klyachin 1990). The narrow absorption lines (called R-lines), overlapping the long-wave spin-allowed band (the most intense line at 684 nm or 14620 cm^{-1}) are caused by spin-forbidden transitions of $^{[vi]}Cr^{3+}$. By gemological definition beryl is considered as emerald only when the narrow R-lines, especially the most intense one at 684 nm, is discernable in a visual gemological spectroscope (Anderson 1990). The absorption lines in the spectrum of sample #18 unambiguously proof that Cr^{3+} substitutes for Al^{3+}.

A series of sharp narrow absorption lines in the NIR-range in both E||**c**- and E⊥**c**-polarization is caused by overtones and combined vibrations of H_2O molecules. The general features of the spectrum indicate the predominance of type II water, i.e. the water molecules in the structural channels neighboring large alkali ions (Wood and Nassau 1968).

In the diffuse reflectance spectrum of sample #16 (Fig. 9b) there are absorption bands and lines of Cr^{3+}, close in energy and shape to those in the absorption spectrum of sample #18 (Fig. 9a). Furthermore, at around ~830 nm there is a broad intense band, which in an unpolarized reflectance spectrum indicates the predominance of the E⊥**c**-polarized band of $^{[iv]}Fe^{2+}$, substituting for Be ions in the distorted tetrahedral sites of the structure. The sharp narrow lines of water vibrations are not seen, since the most intense of them are beyond the spectral range studied (cf. Fig. 9).

The FTIR spectrum measured in the range 6000-1500 cm^{-1} in polarization *E*||**c** consists of three very intense bands caused by fundamental vibrations of H_2O molecules captured in two different positions in beryl channels. They are centered at 1632 and 1620 (double peak), at 3592 and 3698 cm^{-1}, and weaker bands at 3234, 3346, 3522, 3984, and 5274 cm^{-1} (Fig. 10a-c). The narrow band with maximum at 3698 cm^{-1} is due to ν_3 asymmetrical stretching mode of H_2O I molecules with symmetry axis ⊥**c**; the more intense and broad band at 3592 cm^{-1} represents ν_1 symmetric stretching and the double peak in vicinity 1630-1620 cm^{-1} represents ν_2 bending modes of H_2O II molecules with symmetry axis ||**c** (e.g. Wood and Nassau 1968; Goldman et al. 1977; Łodziński et al. 2005).

The IR spectrum measured in polarization *E*⊥**c** consists of a very strong and broad envelope with maximum near 3655 cm^{-1}, medium to weak bands at 5274, 3607, 3593, 1710, 1635 with a broad shoulder at 1655, 1600, and 1545 cm^{-1}. The central envelope near 3655 cm^{-1} represents ν_3 asymmetrical stretching vibrations of H_2O II. Three bands in the middle IR region (a narrow one at 1600 cm^{-1}, a broad shoulder at 1655 cm^{-1}, and a band at 1545 cm^{-1}) are the central ν_2 bending mode of H_2O I and their symmetrically spaced satellites, caused by combining with H_2O rotation

frequency (Wood and Nassau 1968). A broad band near 1930 cm^{-1} in both polarizations is the first vibrational overtone from the silicate ring (Taran et al. 2017).

In addition, we found a narrow, strongly polarized $E \perp \mathbf{c}$ band at 2359 cm^{-1} (Fig. 10d) indicative of relatively high amounts of CO_2 in the channels, which is not common for most beryls. Assignments of all vibrational bands mentioned here are based on classical interpretation by Wood and Nassau (1968) and on our data from a diverse collection of beryls and ring silicates (e.g. Taran et al. 2017).

Be-Li determination of other emerald samples

The Be contents of the selected emerald samples determined by SIMS (Table 2) span a considerable range from 12.7 to 13.9 wt% BeO, the maximum close to the values for ideal anhydrous beryl (13.96 wt%) or 13.51 wt% for hydrous beryl with 1 H_2O pfu (corresponding to 3.24 wt%); the low values were obtained from crystals with a large amount of substitution at the octahedral position. Within a given crystal, core and rim analyses differ only slightly.

Li-contents determined by SIMS (Table 2) for two crystals (Ural Mts.) are between 0.2 and 0.4 wt%, for the other crystals on the order of 0.02 to 0.07 wt%. The analyses with higher Li-content have the same order of magnitude as do the Li_2O-determinations made by dissolution and spectrometry; for crystal 78-14 the SIMS values are slightly higher, for sample 78-78 they are slightly lower.

Other elements contents determined by EPMA (Table EA 3), such as Cr, V, Fe, Mg, and alkalies, are consistent with the range of results reported in the literature. Water contents for selected samples are all between 2.07 and 2.31 wt%. Calculated mineral formulae, based on 18 oxygen atoms, are presented in Table 4. Cations were assigned to positions in the structure according to the following sequence: All Si is attributed to the Si_6O_{18}-ring; excess Si is placed into the Be-tetrahedron. If Si is < 6.000 apfu, it is filled with small amounts (0.01 to 0.05 apfu) of ^{iv}Al and ^{iv}Be (sample 78-78, Ural Mts.) or with ^{iv}Al only (sample 78-14, Ural Mts.).

The Be tetrahedra are then filled with between 2.920 to 3.000 Be; any small deficit is filled with ^{iv}Li. Most samples have ≤0.008 apfu ^{iv}Li, except for some analysis (rim 78-14 Ural Mts., 78-16 South Africa, rim 80-47 Austria), which all have 0.025 apfu ^{iv}Li. To fill the Be-site completely, small amounts of 0.010 to 0.075 ^{iv}Al are necessary. The rest of Al together with Mg, Fe^{2+}_{tot}, Mn, Cr, V, Ti, and traces of Ca are assigned to the Al-octahedral site, which is finally filled with ^{vi}Li to achieve a value of 2.000. Excess Li for the samples from Ural Mts. is then assigned as ^{ch}Li (channel site), together with Na, Cs, and traces of K. The formulae and uncertainties are discussed below.

DISCUSSION

SIMS data and substitutions involving Si-Be-Li

The calculated formulae for emeralds, for which Be and Li contents were determined by SIMS, are listed in Table 4 together with the analyses of emerald from the data set of Aurisicchio et al. (1988) (based on Be- and Li-analyses by wet chemistry, other elements by EPMA combined with single XRD refinement). Some of their emerald crystals are from the same localities as studied here (Colombia, Russia, Austria); the two data sets agree well. Almost all crystals show a slight excess of Si, which is attributed to the Be site, up to 0.049 apfu (Table 4), with the exception of the crystals from Ural Mts., which show a deficit with values of between 5.942 and 5.977 Si apfu. An error in the SiO_2-determination of 1% relative (i.e. approximately ±0.7 wt% SiO_2) translates into a range of approximately ±0.005 Si apfu. Therefore an excess of ~0.05 Si apfu is significant. In our site assignement, a deficit in Si is compensated by Be and Al (crystal #78-78) or by Al alone (78-14; 80-47r). The crystal #78-78 is unusual, because it is the only one with Be > 3.000 apfu: Be of 3.031 and 3.082 apfu for core and rim analyses, respectively. It is also the crystal with the highest amount of Li (0.105 apfu) in the entire data set. All other crystals show a slight deficit of Be (lowest value of 2.870 apfu, Table 4 for a crystal from Brazil; Aurisicchio et al. 1988). This deficit is balanced by a combination of tetrahedral Li, Al, and Si with the highest values for Li (0.037 apfu) and Al (0.085 apfu) for the crystal from Brazil. Thus, in all emeralds except those from Ural Mts., Li is exclusively situated at the Be-site. In order to fulfill the assumption that the octahedral position must be filled with 2.000 apfu and the Be-site with 3.000 apfu (no vacancies), in the Ural Mts. emeralds Li must be partly housed in the octahedral and in the channel position.

A critical parameter for the formula calculation is the uncertainty of the SiO_2-determination, because with *circa* 64 wt% it dominates the chemical composition. We assume an uncertainty for the SiO_2-determination of 1% relative for both Si and for BeO, which is twice the estimated uncertainty of the Be determination. One thing to remember is that the relative uncertainty on the Si is fully propagated onto the SIMS Be values. Hence, Be uncertainty can never be as good as that for Si in relative terms. A calculated formula with a corrected value for SiO_2 by +0.5 wt% and for BeO by -0.14 wt% for crystal # 78-78 still yields a Si-deficit of 0.039 apfu and a Be excess of 0.011 apfu (average for core and rim). For both the uncorrected and the corrected formulae, there is no site available for tetrahedral Li, and it can only be partially accommodated by the octahedral sites; some Li must be assigned to the channel position, because the octahedral site is completely filled with tri- and divalent cations. The core and rim analyses of the second crystal from Ural Mts. (78-14) have only a small Si deficit of 0.015 and 0.023 apfu, filled by ^{iv}Al, and for Be of 0.025 and 0.002 apfu, filled by ^{iv}Li. For these domains the Li must be accommodated as ^{vi}Li and ^{ch}Li. Similarly, crystal #26 (Ural Mts.; from Aurisicchio et al., 1988) has the octahedral position filled with 2.003 apfu, some Li (0.020 apfu) is tetrahedral, and the rest of Li (0.019 apfu) must be assigned to the channel position.

None of the other emeralds discussed here show such peculiarities. In summary, the available data (Table 4) confirm that for emeralds the Si-site is mostly filled with Si, i.e. there is no Tschermaks substitution, only small excesses or deficits are possible as seen in crystals from Ural Mts. and Habachtal. The Be-site shows mostly a small deficit, only our crystal 78-78 from Ural Mts. has excess Be (assigned to the Si-site). The observed small amounts of Li are in most cases accommodated at the Be-site (Colombia, Austria, Brazil, Mozambique, Pakistan), only for the crystals from Ural Mts. it is partly distributed to the octahedral- and the channel sites. These data also agree with those from Aurisicchio et al. (2018) with SIMS data for Be and Li, although in that study the analytical uncertainties for Be (5% rel.) and Li (10% rel.) are too large to confidently assign small amounts to specific crystal sites.

The general procedure analyzing beryls is that Be-contents are not determined and formulae were calculated assuming the theoretical content of 3.000 Be apfu. Because we want to check this procedure for beryl with unknown Be-contents, we also calculated a theoretical BeO_{calc} content from the EPMA of these samples (Fig. 11). For most of the crystals the calculated contents are too high by ~0.2 wt%, and a similar relation is found in the data set of Aurisicchio et al. (1988). Only in the case of the anomalous crystal from Ural Mts. (78-78; Table 4) is the measured BeO content higher than the calculated one.

By combining our SIMS-data for Be and the EPMA analyses for the SiO_2-contents we can confirm that Be = 3.000 is a good first assumption for all emeralds (Fig. 12). A regression line (wt% BeO = 0.2281*wt% SiO_2 - 1.3239; R^2 = 0.927) calculated from all our own analytical data (Table EA 4) is almost identical to the line that connects the ideal beryl and hydrous beryl compositions. If the calculated BeO content is higher, as for the Kruta Balka (Ukraine), the Mavis Lake (Canada) and Manyara (Madagascar) deposits, a slightly lower Be-site occupation is implied. The effect of Fe-substitution ('ideal hydrous Fe-end-member') is negligible, as long as the total amount of Fe is low, as is the case for most emeralds. Analyses plotting below the line (such as Norway and Um Kabu, Sikait, and Zabara from Egypt) are characterized by Si values that are significantly higher than 6.000 apfu.

The Kruta Balka occurrence

The chemical composition of the beryls from Kruta Balka and their spectroscopic characteristics clearly show that they are emeralds, both in the popular usage (Conklin 2002) and in a mineralogical strict sense (Anderson 1990; Schwarz and Schmetzer 2002). In the NIR range, polarized broad bands at ~800-1000 nm are also characteristic of emerald from most deposits, aside from some almost iron-free crystals from Muzo and Chivor in Columbia (e.g. Tretyakova and Benavides 1987, found in such emeralds only 0.01 wt% FeO). These bands (Figs. 7 and 8) are

caused by electronic spin-allowed transitions of Fe^{2+} in both octahedral (Al^{3+}) and tetrahedral (Be^{2+}) sites (e.g. Wood and Nassau 1968). The former one causes the doublet-structured E||**c**-polarized band, split by Jahn-Teller effect with maxima at around 850 and 1000 nm, the latter causes a more intense E⊥**c**-polarized single band at around 830 nm. The presence of these features in the spectra from the Kruta Balka samples is consistent with the microprobe data (Tab. 3), which show up to 0.5 wt% FeO_{tot}. Note that a relatively high intensity of the absorption bands of Fe^{2+}, when their short-wave tail reaches the visible range, may contribute to a bluish hue of the green color of the sample. We can roughly estimate both $^{Be}Fe^{2+}$- and $^{Al}Fe^{2+}$-content from the spectra as ~0.004 and ~0.008 apfu, respectively (Taran and Vyshnevskyi 2019). The Fe^{3+}-content cannot be estimated, because a weak spin-forbidden band of the ion at ~26.820 cm^{-1}, used for that is hidden by an absorption edge and broad band of Cr^{3+}. There can also be some $^{Be}Fe^{3+}$, less than $^{Be}Fe^{2+}$, which again we are unable to quantify.

Comparing the calculated BeO content of the Kruta Balka emerald analyses with the measured SiO_2 content (Fig. 12), they plot above the line connecting the ideal with the substituted beryls (Fig. 12). This indicates either an over-determination of the calculated BeO content or an underestimation of the SiO_2 content by EPMA. However, since both methods (WDS and EDS) with three different instruments on three different crystals yielded similar results for SiO_2, underestimation seems unlikely, suggesting that in these emeralds the Be-content is possibly slightly below 3.000. The formula calculated with a value corrected by -0.30 wt% BeO (taken from Fig. 12) and with the average Li_2O content for beryl from Kruta Balka (Rozanov and Lavrinenko 1979), yields 2.944 Be apfu.

The infrared spectra of beryl show the presence of both types H_2O I and H_2O II in the channels. Clearly observable structures in the vicinities of ν_2 and ν_1 bands of H_2O II lead us to conclude that both are represented by envelopes formed from at least two overlapping separate narrower bands. For ν_2 their maxima are located at 1620 and 1632 cm^{-1} (Fig. 10c), and at 3600, 3592 with a shoulder at 3585 cm^{-1} for ν_1. Fukuda and Shinoda (2008) proposed that Na-associated water molecules in beryl may exist in two configurations, either as doubly coordinated H_2O-Na-OH_2 (H_2O IId), or as singly coordinated H_2O-Na (H_2O IIs). They assumed that in the case of H_2O IId, a ν_2 band has its maximum at 1620 to 1624 cm^{-1} and ν_3 band at 3660 to 3664 cm^{-1}, while the same bands of H_2O IIs are centered at 1633 to 1637 and 3643 cm^{-1}, respectively (Fukuda and Shinoda 2008; Fridrichova et al. 2016). Thus, we assign the peak at 1620 cm^{-1} to vibrations of H_2O IId, whereas the ν_2 maxima at 1632 cm^{-1} is assigned to H_2O IIs. The position of the central point of the broad ν_3 band at 3655 cm^{-1} is also situated between predicted wave numbers for pure H_2O IId and H_2O IIs configurations. This indicates that the amounts of H_2O II molecules in both configurations are nearly equal. Taking the dominant intensities of H_2O II bands into consideration, we can assume that this species is much

more (at least 2 times) abundant compared to H_2O I. Total water content was not analyzed, but through a comparison of respective bands' intensities (Fig. 10a-c) with those in the spectra of samples with known water content (Table EA 4) we estimate about 1.5 wt% of total H_2O in the KB samples.

With these values, the 'best estimate' for the crystal chemical formula for the KB emeralds is $(Na_{.324}K_{.004}Cs_{.020}Li_{.016})_{0.364}(Al_{1.815}Cr_{.015}V_{.004}Fe^{2+}_{.018}Mg_{.063}Mn_{.002}Ca_{.002}Ti_{.001}Li_{.076})_{2.000}[Be_{2.944}Li_{0.056}Si_{5.937}Al_{0.063}O_{18}]H_2O_{0.920}$, neglecting small amonts of Fe^{2+} at the Be-site and Fe^{3+}. The very high Na contents are likely explained by a combination of the tetrahedral substitution $LiNaBe_{-1}\square_{-1}$ and the octahedral substitution $LiNa_2Al_{-1}\square_{-2}$. As shown above that the tetrahedral substitution accounts for 0.056 Be apfu, but the total amount of Na(+K+Cs) is 0.349 apfu, which leaves enough Na for charge compensation for $LiNa_2Al_{-1}\square_{-2}$.

The estimated H_2O content of 1.5 wt% (from FTIR), equivalent to 0.920 H_2O pfu, is consistent with the total amount of H_2O II bound to Na^+ (H_2O IId + H_2O IIc). This value is low compared to emeralds worldwide and does not fit the generally observed correlation between Na_2O and H_2O (Marshall et al. 2016), which is based on the crystal-chemical argument of the combination of Na with H_2O molecules (e.g. Hawthorne and Černý 1977). However, experimental data (Pankrath and Langer 2001) clearly show that the water content in Na-free beryl is a function of P_{H2O} and T; thus the Na-content is a complex function of P, T, crystal chemistry and the presence of other Na-bearing phases (e.g. albite, tourmaline, fluid; see discussion below). Unquantified amounts of CO_2 were identified as a narrow band at 2359 cm^{-1}, in the same range as first reported by Wood and Nasssa (1967) for CO_2 molecules in the channels. In the absence of fluid inclusion data there is no clear indication for the source of CO_2, but the geological situation at Kruta Balka with carbonates among the country rocks suggests metamorphic fluids.

The **c/a** ratio of the KB emerald of 0.999 classifies them as 'tetrahedrally substituted' beryls in the nomenclature of Aurisicchio et al. (1988), although the chemical composition requires that substitution of Li at the octahedral position is equally important; in addition, some Li must be assigned to the channel position. Within the channels, Li likely occupies the 2b-position with a planar [6]-fold coordination and a distance to oxygen O_1 of 2.548 Å (Hawthorne and Černý 1977). The 2a-site with a [12]-fold coordination is much too large, and such a high coordination number has not been observed in Li-compounds (Gagné and Hawthorne 2016). Hawthorne and Černý (1977) also assigned 0.049 Li apfu to the 2b site in their crystal structure refinement of a Cs-Li beryl.

The Li for KB emeralds is sourced from pegmatites, which are rich in Li, as indicated by the presence of spodumene and petalite, and the Li-bearing tourmaline inclusions in emeralds. Emeralds from Crabtree Mts, USA are also from a locality with spodumene-bearing pegmatites

(Wise and Anderson 2006), and they are also closely associated with tourmaline. The high Hf-content of zircon inclusions (up to 11 wt% HfO_2) is consistent with the association of the KB emeralds to albite-spodumene pegmatites with a complex Be-Li-Cs-Ta-mineralization; high-Hf zircons are characteristic for pegmatites with Ta-Nb-mineralization (Speer 1982).

Substitutions in emeralds and Cr-V sources for emerald

In order to compare the KB emeralds with other deposits we compiled critical major element values from all to us known localities worldwide (Table 5; complete data set in Table EA 6). This data reveals a wide range in Al_2O_3 contents ranging between ~11 and 19 wt%. The calculated content of wt% BeO, assuming 3.000 Be apfu for all these analyses, varies between ~13 and 14 wt%. We use these data together with the determined SiO_2 contents by EPMA (Fig. 12) to show if the assumption of 3.000 Be apfu is robust. Figure 12 also shows the ideal compositions for both beryl and other possible end-members, as well as reference data from a relatively pure beryl from a pegmatite (Table EA 3) and data from emerald and synthetic beryl reported on by Aurisicchio et al. (1988). All data should lie between ideal beryl and these end-members. The theoretical values for ideal beryl (hydrous and anhydrous), femag-beryl (shown for hydrated Fe and Mg end-members) and for Li-octahedrally substituted beryl $LiNa_2Al_{-1}\square_{-2}$ lie on a line, because the ratio BeO:SiO_2 does not vary significantly. However, the tetrahedral substitutions $LiNaBe_{-1}\square_{-1}$ (avdeevite) and $LiCsBe_{-1}\square_{-1}$ (pezzotaite) change the ratio strongly, and due to the high atomic weight of Cs the pezzotaite component also significantly influences the weight percentages of SiO_2 and BeO. In fact, all analyses of emeralds cluster near to the line connecting ideal anhydrous beryl with the hypothetical end-members for hydrated femag-beryl, confirming our assumption. For those, which are off the line a correction needs to be applied.

For a further characterization of emerald composition, we use the Mg# and Cr# as characteristic values. This is based on the original concept for emerald genesis (Fersman 1929), in which Be is supplied by pegmatites, and metasomatic reactions with metamorphosed ultramafic country rocks (serpentinites and others) supplied the chromophore elements Cr and V. Ultramafic-ultrabasic rocks in general are mantle-derived, and therefore their Mg# is restricted to values between ~0.80 and ~0.90. Lower and higher values indicate other sources. Chromium is always concentrated in (metamorphosed) ultramafic-ultrabasic rocks (see e.g. Cawthorn et al. 2005, for enrichment of both elements in mafic and ultramafic rocks), but in common ultramafic rocks V is present only at low concentrations (e.g. Cawthorn et al. 2005), and therefore Cr# in emeralds are high.

The average Mg# of emeralds worldwide (Fig. 13) range from ~0.15 to 0.99, but cluster between 0.80 and 0.90. The average Cr# vary between 0 and 1.0, but most values are ≥0.70. The reader should be aware that the characterization presented here is done with the average *typical* values;

individual analyses may deviate strongly (Fig. 5). Here we refer to localities with Mg# between 0.80 and 0.90 and Cr# ≥0.90 as 'ultramafic' schist type, associated with metamorphosed ultramafic-ultrabasic host rocks.

Metasediments represent another possible source for Cr and V, typically in the form of organic-rich rocks such as blackshales and impure limestones, as they are known organophiles (e.g. Tribovillard et al. 2006). Incorporation of these elements into minerals during metamorphism is well known for garnet and epidote (e.g. Bačík et al. 2017), and for oxide minerals (Di Cecco et al. 2018). In sediments, however, both elements are redox-sensitive, and can become enriched or depleted during diagenetic and metasomatic events, and can be coupled or decoupled, which results in highly variable Cr#. These localities are called 'sedimentary', referring to the sedimentary origin of Cr and V. The best-known examples are the Cordilleran-type emeralds from Colombia. Hewton et al. (2013) discovered a similar locality in the Canadian Cordillera (Mc Kenzie Mts.), but also other Canadian localities (Lened with skarn as host rocks, and Yukon territories) belong to this type.

Localities with Mg# between 0.70 and 0.80 and Cr# down to 0.70 are referred to as ‘transitional’, i.e. their host rocks are (meta)ultramafic-basic rocks, which may contain a sedimentary component. For the KB emeralds, this situation is well documented (Fig. 2). Here, country rocks of the pegmatites are both metamorphosed ultramafic rocks and meta-black shales. For each individual sample the Mg# and Cr# depend strongly on the local situation within the deposit.

The Alpine-type localities (from the Alpine-Himalaya-chain) are 'ultramafic' (Habachtal, Austria; Bulgaria) or 'sedimentary' (Binntal, Switzerland; Sharbag-Swat and Gandao, Pakistan; Afghanistan; Kazakhstan). The occurrence at Binntal, Switzerland is hosted in quartz veins and vein breccia fragments within a magnetite-bearing meta-quartzite (Marshall et al. 2017), which provided an extreme Mg# of 0.99. The majority of Gondwana-basement-type localities from Brazil, Africa, Madagascar, Australia, and India are 'ultramafic' or 'transitional', with the exception of Sunbawanga and Manyari (Tanzania), Jos (Nigeria), Salinhina (Brazil), and Emmaville (Australia). Emerald localities from the Eurasian basement settings (Norway; Dyakou, Davdar, in China) are all 'sedimentary'.

In many emeralds the femag substitution $(Mg,Fe^{2+})NaAl_{-1}\square_{-1}$ is dominant (e.g. review by Groat et al. 2008). The maximum degree of femag substitution has been observed for emeralds from Egypt, Madagascar and Brazil (Fig. 14), and so far no indication for a miscibility gap has been reported (see also Aurisicchio et al. 1988). However, there are two clusters of data, and we divide the diagram at a value of 0.250 apfu in two groups with low and high substitutions. Theoretically, the substitution can reach 1 (Mg,Fe) + 1 Na apfu, limited only by the number of 2b channel sites at

the level of the Si-rings. However, Na^+ is generally associated with water positioned within the channels, requiring the water molecule in the channel site 2a to have its negative bipole oriented toward the Na^+ (H_2O II orientation; Wood and Nassau 1968). Therefore, two H^+ near to the next ring would cause extra positive charge, which does not allow Na^+ to occupy this neighboring position, reducing the total amount of Na to 0.5 apfu; this can be considered to represent the end-member of the solid solution. However, only for the samples from Sandawana (Zimbabwe) is Na (+ minor K, Cs) close to 0.500 apfu, for all others it is below 0.400 apfu (Fig. 15). This indicates an additional substitution mechanism for Mg, such as $MgBe_{-1}$ (see below).

Several individual analyses of emeralds from Ianapera, Madagascar (Andrianjakavah et al. 2009) go slightly above this limit (not plotted in Fig. 14). However, these are among the rare emeralds reported that have high K contents (0.156 apfu), even exceeding their Na contents (0.138 apfu). The only other localities with elevated K content are those from Tanzania (Moroz et al. 2002), where up to 0.33 wt% K_2O have been reported. With such large amounts of K in the channel the model above about the water arrangement may no longer be strictly valid.

The fact that in most emeralds the K-content is near the detection limit is astonishing, because the majority of the ultramafic schist-type localities are situated in biotite-rich country rocks, where K-saturation can safely be assumed. We argue therefore that the absence of K in the beryl channel is due to the intermediate size of K^+ between Na^+, which fits well at the 2b ring center position, and Cs^+, which fits well at the 2a position between two rings. The Ianapera emerald locality is situated in an area, where granulite facies conditions were achieved (see Andrianjakavah et al. 2009), and possibly such high *P-T* conditions favored the incorporation of K into the channels of beryl.

A high femag substitution requires saturation with both Mg+Fe and Na. Saturation of Mg+Fe is indicated by the presence of Fe-Mg minerals, predominantly biotite, chlorite, amphibole, talc, and also tourmaline, which is in many deposits a characteristic accessory mineral. In quartz vein assemblages where no Mg-Fe minerals are present, emeralds reveal little or no femag substitution, such as those from Jos, Nigeria (Schwarz et al. 1996; Vapnik and Moroz 2000). They have only 0.08 wt% MgO and in the calculated formula (Al+V+Cr) ~2.000 apfu, with a negligible amount of femag substitution. Thus we conclude that the amount of femag substitution is partly controlled by the local availability of Mg+Fe.

The femag substitution requires the availability of an equivalent amount of Na, and the availability of Na can be another limiting factor for the femag substitution. There are numerous studies of fluid inclusions in emerald, which show a wide range in salinities (see review by Groat et al. 2008) from almost nil (e.g. Swat, Pakistan; Seal 1989) up to 40 wt% $NaCl_{equ}$ (e.g. the Colombian emeralds; Groat et al. 2008). An example, where at a high Mg+Fe whole rock content is associated with a low femag substitution in emerald of only ~0.1 apfu, is our sample from Western Australia

(Fig. 14); the crystal is embedded in a matrix of almost monomineralic phlogopite, such that a saturation in the Mg+Fe component is assured, leading us to postulate a very low concentration of Na in the fluid.

A typical Na-mineral in equilibrium with emerald is tourmaline, which is a key Mg-Fe mineral in Kruta Balka (together with muscovite), Lened (Canada), the Crabtree Mts. (USA), and Debelgetey (Kazakhstan). All these localities belong to the low substitution group. The exchange vector $(Mg,Fe^{2+})NaAl_{-1}\square_{-1}$ also operates in tourmaline [e.g. dravite-schorl $Na(Mg,Fe)_3Al_6Si_6O_{18}(BO_3)_3(OH)_4$ - Mg-foitite-foitite $\square(Mg,Fe)_2Al_6Si_6O_{18}(BO_3)_3(OH)_4$]. If tourmaline crystallized (due to a high B-content in the system) and if it controls the Mg,Fe + Na content in the sample, then there is no Mg,Fe + Na left over for the femag-component in beryl. Experimental studies on tourmaline have shown that this substitution depends strongly on fluid composition, as well as on *P* and *T* (von Goerne et al. 2001, 2011; Berryman et al. 2016). Using the experimental data by von Goerne et al. (2001) about Na-distribution between tourmaline and fluid, a Na-concentration in the fluid of ~0.6 mol L^{-1} Na is calculated for the KB emeralds, with very Ca low concentrations in the fluid (using Ca-poor tourmaline-albite pairs; von Goerne et al. 2011).

For most data there is a fairly strong positive correlation between Mg+Fe and Na (+ minor K, Cs) (Fig. 14). For those analyses which plot above the line for the exchange vector $(Mg,Fe^{2+})NaAl_{-1}\square_{-1}$ a certain amount of Fe^{3+} can be assumed, which shifts many analyses towards the ideal line. However, for a number of localities (Sikait, Zabara, Um Kabu from Egypt; St. Terezinha, Socotó from Brazil; Mananjary, Ianapera, from Madagascar; Chantete, Kagem from Zambia) the data remain above the line, even when all Fe is assumed to be Fe^{3+}, indicating an additional substitution for Al by Mg. This is also seen in Figure 14, where several localities (Manyara, Tanzania; Ianapera, Madagascar; Mariinskoye, Russia; Socotó and Tauá, Brazil) lie above the line for the ideal substitution. This additional component, which does not reduce the Al-content of the beryl, and which does not include Na, is possibly the Be-cordierite component $Mg_2[Al_2BeSi_6O_{18}]$ (Hölscher and Schreyer 1986); the substitution $MgBe_{-1}$ increases the Mg-content but does not change the amount of Al and Si in beryl. For the Tanzania and Madagascar deposits, high-grade metamorphism has been postulated (Moroz et al. 2002; Andrianjakavah et al. 2009), and it is likely that high temperatures should favor this substitution. Analyses below the line (Fig. 14) indicate higher amounts of Na (+K+Cs) and the replacement of Be by Li+Na and Al by Li+2Na; they are significant in the samples from Kruta Balka (Ukraine), Mavis Lake (Canada), Crabtree Mts. (USA), Binntal (Switzerland), and Dyakou (China).

As discussed above, the *P-T* conditions also influence the amount of femag substitution. Emeralds from high-grade Gondwana-type basement localities generally show a high amount of femag substitution. For the Colombian emeralds, low temperature conditions of ≤350°C near to the

lower *P-T*-stability of beryl (Barton and Young 2002) are well constrained (e.g. Pignatelli et al. 2015); a high Na-activity has been established due to the high salinity in fluid inclusions, and Mg+Fe are provided by dolomite and chlorite. For the locality Peñas Blancas in the Eastern Cordillera the amount of femag substitution is ~0.2 apfu (Pignatelli et al. 2015), and thus this is the maximum femag component at low *P-T*. The emeralds from Austria, which crystallized during prograde metamorphism (Grundmann and Morteani 1989), show a systematic core-rim relationship with increasing femag component towards the rim (Franz et al. 1986), correlated with an increasing temperature. Aurisicchio et al. (1988) have shown that with increasing femag substitution the size and distortion of the Al-octahedron increases, and this is consistent with increasing temperature favoring the femag substitution. The effect of pressure might be the opposite, although no data are available for supporting this assumption.

CONCLUSIONS

The analysis of emeralds is simplified by the assumption of 3.000 Be apfu in emerald being in general valid. EPMA are sufficient for a first characterization, despite the fact that Fe^{3+}/Fe^{2+} cannot be distinguished and water contents are unknown. Comparison between the calculated BeO-content with measured SiO_2-contents (Fig. 12) is useful to check this assumption, and only in case of significant deviation from the ideal compositions a correction might be applied or Be measured directly with other methods (e.g. SIMS). Silicon values are mostly near to the ideal value of 6.000 apfu. Because of the low atomic weights of Be and Li, and because of the high amount of SiO_2 in beryl, low analytical uncertainties are required when measuring these elements. Otherwise, no robust conclusions can be made for substitutions involving Si-Be-Li.

Li-contents are in many cases quite important and necessary for calculating a correct mineral formula. If Li-contents are available, normalization to Be+Li = 3.000 apfu is possible, because in most emeralds Li substitutes for Be via $LiNaBe_{-1}\square_{-1}$ (see Table 1 for possible substitutions; Table 4 for cation distribution in selected emeralds). The tetrahedral coordination of Li is also the most frequently observed (Gagné and Hawthorne 2016). Nevertheless, in KB emeralds Li is also observed on the octahedral site, substituting for Al via $LiNa_2Al_{-1}\square_{-2}$ (which is also common in other Li-compounds, Gagné and Hawthorne 2016), and at the channel position 2b, with a planar [6]-coordination. Our data provide more evidence for Li as a minor channel constituent, as discussed for CsLi-beryls (Hawthorne and Černý 1977).

Water molecules (at the 2a position) and Na (at 2b) are common at the channel position in emeralds. The Na-atoms at 2b would be underbonded, if there were no water molecules bonded to Na, which argues for a positive correlation between Na- and water contents, but Na only controls the minimum possible amount of one H_2O molecule bonded to Na (Hawthorne and Černý 1977).

The positive correlation in emeralds, first observed by Zimmermann et al. (1997; refined correlation by Marshall et al. 2016) was used to calculate water contents in emeralds, but it must be used with caution, because even in Na-free synthetic beryls water content increases to 3 wt% as a function of *P* and *T* (Pankrath and Langer 2001).

To explain the anomalous Na-contents of the KB emeralds (likely connected with Li), mapping of the Na-contents has been proven to be extremely useful. The Na-distribution is irregular in a vein-like and patchy network (Fig. 6) and in areas parallel to cracks (Fig. 7), likely correlated with the strong infiltration by Na inducing $LiNa_2Al_{-1}\square_{-2}$ replacement during late-stage hydrothermal activity. Our preliminary comparison of element maps of emeralds from other localities confirms that this method yields important information on the crystallization processes of emeralds.

In most emeralds the femag-component is an important factor controlling the Na-content via $(Mg,Fe^{2+})NaAl_{-1}\square_{-1}$. The maximum of 0.5 Na apfu is however rarely reached; more common is a substitution of up to 0.4 Na apfu (Fig. 15). An apparently higher substitution (Fig. 14) suggests the presence of Fe^{3+} (instead of Fe^{2+}) as the stoppaniite component (Fig. 15) and/or a Be-cordierite component $MgBe_{-1}$. The femag-component is a complex function of *P* and *T*, saturation of Na (controlled by other Na-minerals such as albite and tourmaline, and the fluid phase), and saturation of Mg,Fe^{2+} (mostly controlled by biotite, amphibole, talc, and tourmaline). Again, mapping of the element concentrations (mainly Mg; Figs. 6 and 7) provides valuable information about the growth conditions.

At Kruta Balka the close connection of emerald mineralization to granites and pegmatites strongly suggests that these provided the source of Be and Li. The small amount of femag substitution points to low *P-T* conditions and/or a low Na-concentration in the fluid; tourmaline composition at Kruta Balka indicates ~0.6 mol L^{-1} Na in fluid (compared to the experimental fluid-tourmaline partitioning data by von Goerne et al. 2001) and a very low concentration of Ca in fluid as shown by Ca-poor tourmaline-albite pairs (von Goerne et al. 2011). The replacement structures seen in the cores (Fig. 6) clearly indicate a metasomatic origin, where a Be-bearing fluid possibly replaced an Al-Si-mineral such as feldspar. Inclusions of Hf-rich zircon and Sc-rich apatite are of pegmatitic origin. Sector zoning in the core (Fig. 7) indicates several pulses of growth. The outer part of the crystal, with oscillatory zoning and the highest amount of Cr, Sc, and V (Figs. 6, 7) indicate further growth of emerald and incorporation of these elements from the fluid. Oscillatory zoning of Cr, which is in most cases enriched on the growing prism faces (Fig. 7), is indicative of rapid disequilibrium growth from a fluid.

IMPLICATIONS

The observations resulting from the study of Kruta Balka imply that detailed crystal chemical information combined with the spatial distribution of certain elements can give important

766 indications of what is involved in the genesis of emeralds, which is also the basis for many
767 classification systems. Such information might even allow the otherwise difficult distinction
768 between metamorphic vs. metasomatic deposits where element mobility has been on the thin
769 section scale.

770 A number of different classification schemes have been proposed for emerald deposits, based on
771 their Be source, metamorphic grade, tectonic environment, metasomatic history, and fluid sources
772 as established by their stable isotope signatures (see reviews by Giuliani et al. 1988, 2018; Barton
773 and Young 2002; Schwarz et al. 2002; Groat et al. 2008; Aurisicchio et al. 2018; and references
774 therein). We suggest using the Mg# and Cr# (Fig. 13) of emeralds, which are controlled by their
775 sources, and the amount of femag substitution (Fig. 14) to present a simple characterization of
776 emerald deposits. We have identified three categories of emerald occurrences: (1) the 'ultramafic'
777 schist-type occurrence with Mg# between ~0.80 and ~0.90, and Cr# between 1.0 and 0.8, which is
778 the common one, (2) a 'sedimentary' group, where the source of Mg, Fe, Cr, and V are
779 (meta)sediments such as blackshales and impure limestones, with highly variable Mg# and Cr#, and
780 (3) a 'transitional' group, where the source includes both, ultramafic rocks and metasediments, for
781 which Kruta Balka is an excellent example.

782 This classification serves only as a first step. We propose a subdivision into low (≤0.25 apfu) and
783 high substitution (0.25 - 0.5 apfu) of femag-component. Deposits classified as 'sedimentary' and
784 'transitional' typically show a low femag-component, 'ultramafic' deposits a high femag-component.
785 If emeralds from deposits with a high femag-component, likely connected with the ultramafic schist
786 type, show elevated K contents, they might come from an area with high-grade metamorphism.
787 Pardieu et al. (2015) also used the K-content of emeralds for fingerprinting their origin. Further
788 refinement of the classification (and more information for provenance analysis) could be obtained
789 from trace elements. In addition to the commonly used elements such as Li, Cs and Ga (Aurisicchio
790 et al. 2018; Schwarz 2016), Sc is very promising not only because of a high potential for separation
791 of different deposits (Schwarz 2016), but also for the crystallization history, when analyzing its
792 spatial distribution in a crystal.

793 Furthermore, our data imply that analysis of solid inclusions provide important information for
794 the source of Be. Zircon with an extreme Hf-content is a strong indication of Li-Cs-Ta pegmatites,
795 In addition, tourmaline analysis (which allow calculating a theoretical Li-content) could point to an
796 elevated content of Li in the emeralds. Tourmaline analyses allow obtaining some information
797 about the fluid phase, and in combination with fluid inclusion data (which are often available for
798 emerald studies) tourmaline can assist in deciphering the origin and genesis of emeralds.
799 Knowledge of all this information might also help in prospecting. Assuming that only a small piece

of emerald is available, its analysis can assist in identifying the source rocks, which can then be searched for in the field.

ACKNOWLEDGEMENTS

Special thanks are owed to D. Marshall (Burnaby) for help with literature and for providing access to unpublished data, G. Grundmann (Detmold) for donation of samples from the Habachtal deposits and help in literature research. S. Herting-Agthe (Berlin) supplied many samples from the Mineralogical Museum of TU Berlin, L. Solomatina (Kyiv) supplied samples from Kruta Balka from the Mineral Collection of IGMOF, National Academy of Sciences of Ukraine, and A. Martín Izard (Oviedo) samples from Franqueira, Spain. We thank P. Hörmann (Kiel) for access to his laboratory and help in mesuring Li, and G. Werding (Bochum) for H_2O determination. Helpful reviews of the manuscript by D. Marshall, an anonymous reviewer, and the associated editor E. S. Grew improved the manuscript significantly.

References

Agakhanov, A.A., Stepanenko, D.A., Zubkova, N.V., Pekov, I.V., Pautov, L.A., Kasatkin, A.V., Karpenk V.Y., Agakhanova, V.A., Škoda, R. and Britvin, S.N. (2019) Avdeevite, IMA 2018-109. CNMNC Newsletter No. 47, February 2019, page 143; Mineralogical Magazine, 83, 143–147.

Andrianjakavah, P.R., Salvi, S., Béziat, D., Rakotondrazafy, M., and Giuliani, G. (2009) Proximal and distal styles of pegmatite-related metasomatic emerald mineralization at Ianapera, southern Madagasca Mineralium Deposita 44, 817-835.

Anderson, B.W. (1990) Gem Testing. Butterworths, London, 385 pp.

Aurisicchio, C., Fioravanti, G., Grubessi, O., and Zanazzi, P.F. (1988) Reappraisal of the crystal chemistr of beryl. American Mineralogist 73, 826-837.

Aurisicchio, C., Conte, A.M., Medeghini, L., Ottolini L., and C. De Vito, C. (2018) Major and trace element geochemistry of emerald from several deposits: Implications for genetic models and classification schemes. Ore Geology Reviews, 94, 351-366.

Bačík, P., Uher, P., Kozáková, P., Števko, M., Ozdín, D., and Vaculovič, T. (2017) Vanadian and chromia garnet- and epidote-supergroup minerals in metamorphosed Paleozoic black shales from Čierna Lehota Strážovské vrchy Mts., Slovakia, crystal chemistry and evolution. Mineralogical Magazine, DOI, 10.1180/minmag.2017.081.068.

Barton, M.D., and Young, S. (2002) Non-pegmatitic deposits of beryllium, Mineralogy, geology, phase equilibria and origin. Reviews in Mineralogy and Geochemistry 50, 591-691.

Berryman, E., Wunder, B., Rhede, D., Schettler, G., Franz, G., and Heinrich, W. (2016) P–T–X controls c

Ca and Na distribution between Mg–Al tourmaline and fluid. Contributions to Mineralogy and Petrology 171, 1-31.

Beus, A.A. (1966) Geochemistry of beryllium and genetic types of beryllium deposits. W. H. Freeman and Co., San Francisco and London, 1966, pp. 401.

Brand, A.A., Groat, L.A., Linnen, R. L., Garland, M.I., Breaks, F.W., and Giuliani, G. (2009) Emerald mineralization associated with the Mavis Lake pegmatite group, near Dryden, Ontario. Canadian Mineralogist 47, 315-336.

Cawthorn, R.G., Barnes, S.J., Ballhaus, C., and Malitch, K.N. (2005) Platinum Group Element, Chromiur and Vanadium Deposits in Mafic and Ultramafic Rocks. Economic Geology 100th Anniversary Volume, 215-249.

Černý, P. (2002) Mineralogy of beryllium in granitic pegmatites. Reviews in Mineralogy and Geochemistry, 50, 405-444.

Chornokur, I.G., and Yaskevych, T.B. (2010) Some new data on the geological structure of the area of rare metal deposits Balka Kruta. Mineral Resources of Ukraine, 2, 18-24 (in Ukrainian).

Claesson, S., Bibikova, E., Bogdanova, S., and Skobelev, V. (2006) Archaean terranes, Palaeoproterozoic reworking and accretion in the Ukrainian Shield, East European Craton. In Gee, D. G. & Stephendson, R. A. (eds) 2006. European Lithosphere Dynamics. Geological Society, London, Memoirs, 32, 645–654.

Conclin, L.H. (2002) What is emerald? Fact and opinion. extraLapis English No.2, Emerald, Lapis International, East Hampton, 72-73.

Di Cecco, V.E., Tait, K.T., Spooner, E.T.C., and Scherba, C. (2018) The vanadium-bearing oxide minerals of the Green Giant vanadium-graphite deposit, southwest Madagascar. Canadian Mineralogist, 56, 247-258.

Eidth, T., and Schwarz, D. (1988) Die brasilianischen Smaragde und ihre Vorkommen: Carnaíba/Bahia. Zeitschrift der Deutschen Gemmolgischen Gesellschaft, 37, 31-47.

Evdokimova, O.A., Belokoneva, E.L., and Urusov, V.S. (1989) Determination of the location of impurities in emerald from the data on precision refinement and analysis of the distribution of deformation electron density. Doklady Akad Nauk 306, 95-99.

Feklichev, V.G. (1964) Beryl. Moscow, Nauka (in Russian).

Fersman, A.E. (1929) Geochemische Migration der Elemente. Abhandlungen Praktische Geologie Bergwirtschaftslehre, 18, 74–116.

Franz, G., Grundmann, G., and Ackermand, D. (1986) Rock-forming beryl from a regional metamorphic terrain (Tauern Window, Austria), Paragenesis and crystal chemistry. Tschermaks Mineralogische Petrographische Mitteilungen 35, 167-192.

Fridrichová J., Bačík, P., Bizovská, V., Libowitzky, E., Škoda, R., Uher, P., D.Ozdín, and Števko, M. (2016) Spectroscopic and bond-topological investigation of interstitial volatiles in beryl from Slovakia. Physic and Chemistry of Minerals, 43, 419-437.

Fukuda, J., and Shinoda, K. (2008) Water molecules in beryl and cordierite: high-temperature vibrational behavior, dehydration, and coordination to cations. Physics and Chemistry of Minerals, 38:469–481.

Gagné, O.C., and Hawthorne, F.C. (2016). Bond-length distrubutions for ions bonded to oxygen: alkali ar alkaline-earth metals. Acta Crystallographica, B72, 602-625.

Gavrilenko, E.V., and Dashevskaya, D.M. (1998) Features of emeralds of different genesis and their diagnostic significance. Zapiski RMO (Proceedings of the Russian Mineralogical Society), 127(1), 47-57 (in Russian).

Gibbs, G.V., Breck, D.W., and Meagher, E.P. (1968) Structural refinement of hydrous and anhydrous synthetic beryl and emerald. Lithos, 1, 275-285.

Giuliani, G., France-Lanord, C., Coget, P., Cheilletz, A., Branquet, Y., Giard, A., Martin-Izard, D., Alexandrov, P., and Piat, D. H. (1998). Oxygen isotope systematics of emerald: relevance for its origir and geological significance. Mineralium Deposita, 33, 513-519.

Giuliani, G., Groat, L. A., Marshall, D., Fallick, A., and Branquet, Y. (2018). Emerald deposits: A review and enhanced classification. Minerals, 9, 1-63.

Goldman, D.S., Rossman, G.R., and Dollase, W.A. (1977) Channel constituents in cordierite. American Mineralogist, 62, 1144–1157.

Groat, L.A., Marshall, D.D., Giuliani, G., Murphy, D.C., Piercy, S.J., Jambor, J.L., Mortensen, J.K., Ercit T.S., Gault, R.A., Mattey, D.P., Schwarz, D., Maluski, H., Wise, M.A., Wengzynowski, W., and Eaton D.W. (2002) Mineralogical and geochemical study of the Regal Ridge emerald showing. Canadian Mineralogist, 40, 1313-1338.

Groat, L.A., Giuliani, G., Marshall, D.D., and Turner, D. (2008) Emerald deposits and occurrences, a review. Ore Geology Reviews, 34, 87-112.

Gromov, A.V, Granadchikova, B.G., and Andreenko, E.D. (1990) Typomorphic features of emeralds of some deposits of the world. Zapiski RMO (Proceedings of the Russian Mineralogical Society), 119, 102-112 (in Russian).

Grundmann, G., and Morteani, G. (1989) Emerald mineralization during regional metamorphism, The Habachtal (Austria) and Leydsdorp (Transvaal, South Africa) deposits. Economic Geology, 84, 1835-1849.

Grundmann, G., and Morteani, G. (2008) Multi-stage emerald formation during Pan-African regional metamorphism, the Zabara, Sikait, Umm Kabo deposits, South Eastern desert of Egypt. Journal of African Earth Sciences, 50, 168-187.

Hänni, H.A., Schwarz, D., and Fischer, M. (1987) Die Smaragde der Belmont-Mine bei Itabira, Minas Gerais, Brasilien: Vorkommen und Charakteristika. Zeitschrift der Deutschen Gemmolgischen Gesellschaft, 36, 33-49.

Hawthorne, F. C., and Černý P. (1977). "The alkali-metal positions in Cs-Li beryl." Canadian Mineralogi 15, 414-421.

Hawthorne, F.C., and Huminicki, D.M.C. (2002) The crystal chemistry of beryllium. Reviews in Mineralogy and Geochemistry, 50, 333-404.

Hewton, M.I., Marshall, D.D., Ootes, L., Loughrey, L.E., and Dreaser, R.A. (2013) Colombian-style emerald mineralization in the northern Canadian Cordillera: integration into a regional Paleozoic fluid flow regime. Canadian Journal Earth Sciences, 50, 857-871.

Hölscher, A., and Schreyer, W. (1989) A new synthetic hexagonal BeMg-cordierite, $Mg_2Al_2BeSi_6O_{18}$, an its relationship to Mg-cordierite. European Journal of Mineralogy, 1, 21-37.

Kochelek, K.A., McMillan, N.J., McManus, C.E., and Daniel, D.L. (2015) Provenance determination of sapphires and rubies using laser-induced breakdown spectroscopy and multivariate analysis. American Mineralogist, 100, 1921-1931.

Lake, D.J., Groat, L.A., Falck, H., Mulja, T., Cempírek, J., Kontak, D., Marshall, D., Giuliani, G., and Fayek, M. (2017) Genesis of emerald-bearing quartz veins associated with the Lened W-skarn mineralization, Northwest Territories, Canada. Canadian Mineralogist, 55, 561-593.

Laurs, B.M., Dilles, J.H., and Snee, L.W. (1996) Emerald mineralization and metasomatism of amphibolite, Khaltaro granitic pegmatite-hydrothermal vein system, Harmosh Mountains, Northern Pakistan. Canadian Mineralogist, 34, 1253-1286.

Łodziński, M., Sitarz, M., Stec, K., Kozanecki, M., Fojud, Z., and Jurga, S. (2005) ICP, IR, Raman, NMR investigations of beryls from pegmatites of the Sudety Mts. Journal of Molecular Structure, 744,1005–1015.

Loughrey, L., Marshall, D.D., Jones, P., Millsteed, P., and Main, A. (2012). Pressure-temperature-fluid constraints for the Emmaville-Torrington emerald deposit, New South Wales, Australia, fluid inclusion and stable isotope studies. Central European Journal of Geosciences, 4, 287-299.

Loughrey, L., Marshall, D.D., Ihlen, P., and Jones, P. (2013) Boiling as a mechanism for colour zonations observed at the Byrud emerald deposit, Eidsvoll, Norway, fluid inclusion, stable isotope and Ar–Ar studies. Geofluids, 13, 542-558.

Marshall, D.D., Groat, L.A., Falck, H., Giuliani, G., and Neufeld, H. (2004) The Lened emerald prospect, Northwest Territories, Canada, Insights from fluid inclusions and stable isotopes, with implications for northern cordilleran emerald. Canadian Mineralogist, 42, 1523-1539.

Marshall, D.D., Pardieu, V., Loughrey, L., Jones, A.P., and Xue, G. (2012) Conditions for emerald formation at Davdar, China, fluid inclusion, trace element and stable isotope studies. Mineralogical Magazine, 76, 213-226.

Marshall, D.D., Downes, P.J., Ellis, S., Greene, R., and Loughrey, L. (2016). Pressure–Temperature–Flui Constraints for the Poona Emerald Deposits, Western Australia: Fluid inclusion and stable isotope studies. Minerals 6, 1-22.

Marshall, D., Meisser, N., Ellis, S., Jones, P., Bussy, F., and Mumenthaler, T. (2017) Formational conditions for the Binntal emerald occurrence, Valais, Switzerland, Fluid inclusion, chemical composition and stable isotope studies. Canadian Mineralogist, 55, 725-741.

Martín-Izard, M., Paniagua, A., Moreiras, D., Acevedo, R.D. and Marcos-Pascual, C. (1995). Metasomatism at a granitic pegmatite-dunite contact in Galicia: The Franqueira occurrence of chrysoberyl (alexandrite), emerald, and phenakite. Canadian Mineralogist 33, 775-792.

Moroz, I., Vapnik, Y., Eliezri, I., and Roth, M. (2002) Mineral and fluid inclusion study of emeralds from the Lake Manyara and Sumbawanga deposits, Tanzania. Journal of African Earth Sciences, 33, 377-39

Morteani, G., and Rhede, D. (2017) The multi-fluid metasomatic genesis of the Archean Poona emerald deposit (Murchison Province, Western Australia), microtextures, geochemistry and stable oxygen isotopes. Periodico di Mineralogia 86, 279-300.

Nwe, Y.Y., and Morteani, G. (1993) Fluid evolution in the H_2O-CH_4-CO_2-NaCl system during emerald mineralization at Gravelotte, Murchison Greenstone Belt, Northeast Transvaal, South Africa. Geochimica et Cosmochimica Acta, 57, 89-103.

Pankrath, R., and Langer, K. (2001). Molecular water in beryl, $Al_2Be_3Si_6O_{18}.nH_2O$, as a function of pressure and temperature, an experimental study. American Mineralogist, 87, 238-244.

Pignatelli, I., Giuliani, G., Ohnenstetter, D., Agrosì, G., Mathieu, S., Morlot, C., and Branquet ,Y. (2015) Colombian trapiche emeralds: Recent advances in understanding their formation. Gems & Gemology, 51, 222-259.

Platonov, A.N., Taran, M.N., Polshin, E.V., and Minko, O.E. (1979) The nature of the color of iron-containing beryls. Izvestia Academii nauk SSSR, Geological series 10, 54-68 (in Russian).

Rozanov, K.I., and Lavrinenko, L.F. (1979) Rare-metal pegmatites of Ukraine. Moscow, Nauka (in Russian).

Renfro, N., Sun Z., Nemeth M., Vertriest W., Raynaud V., and Weeramonkhonlert, V. (2017) A new discovery of emeralds from Ethiopia. Gems & Gemology, 53, 114-116.

Santiago, J.S., da Silva Souza, V., de Carvaljho Filgueiras, B., and Cuadros Jiménez, F.A. (2018) Emerald from the Fazenda Bonfim Deposit, northeastern Brazil: chemical, fluid inclusions and oxygen isotope data. 10.1590/2317-4889201820170130 Brazilian Journal of Geology, 1-14.

Schaller, W.T., Stevens, R.E., and Jahns, R.H. (1962) An unusual beryl from Arizona. American Mineralogist, 47, 672-699.

Schwarz, D. (1990) Die brasilianischen Smaragde und ihre Vorkommen: Santa Terezinha de Goiás/GO. Zeitschrift der Deutschen Gemmologischen Gesellschaft, 39, 13-44.

977 Schwarz, D. (1991) Die chemischen Eigenschaften der Smaragde II, Australien und Norwegen.
978 Zeitschrift der Deutschen Gemmologischen Gesellschaft, 40, 39-66
979 Schwarz, D. (2016). The geographic origin determination of emeralds. InColor, 31, 98-105.
980 Schwarz, D., and Schmetzer, K. (2002) The definiton of emerald - The green variety of beryl
981 colored by chromium and vanadium. extraLapis English No.2, Emerald, Lapis International,
982 East Hampton, 74-78.
983 Schwarz, D., Eidth, T., and Couto, P.A. (1988a). Die Smaragde des Minengebietes Socotó, Bahia,
984 Brasilien: Vorkommen und Charakteristika. Zeitschrift der Deutschen Gemmologischen Gesesllschaft,
985 37, 89-112.
986 Schwarz, D., Hänni, H.A., Martins Jr., F.L., and Fischer, M. (1988b). Die Smaragde der Fazenda Boa
987 Esperança bei Tauá, Ceará, Brasilien: Vorkommen und Charakterisitka. Zeitschrift der Deutschen
988 Gemmologischen Gesesllschaft, 36, 133-147.
989 Schwarz, D., Eidt Th., and Couto, P.A. (1990) The Brazilian emeralds and their occurrences:
990 Socotó, Bahia. Journal of Gemmology, 22, 147-163.
991 Schwarz, D., Giuliani, G., Grundmann, G., and Glas, M. (2002). The origin of emerald. Lapis Internationa
992 LLC, East Hampton (extraLapis English, No. 2: Emeralds of the world), 18-23.
993 Seal II, R.R., (1989) A reconnaissance study of the fluid inclusion geochemistry of the emerald
994 deposits of Pakistan and Afghanistan. In Kazmi, A.H., Snee, L.W. (Eds.), Emeralds of Pakistan.
995 Van Nostrand Reinhold, New York, pp. 151–164.
996 Shatalov, N.N. (2017), Tectonics of the Kruta Balka ore knot of the Near-Azovian area. Reports
997 of the National Academy of Sciences of Ukraine, 4, 55-62 (in Russian).
998 Speer, J. A. (1982) Zircon. Reviews in Mineralogy and Geochemistry, 5, 67-135
999 Taran, M.N., and Klyakhin, V.A. (1990) Spectroscopic and colorimetric study of
1000 hydrothermal synthetic emeralds of various compositions. Zapiski RMO (Proceedings of
1001 the Russian Mineralogical Society), 119, 81-93 (in Russian).
1002 Taran, M.N., and Langer, K. (2001) Electronic absorption spectra of Fe^{2+} ions in oxygen-
1003 based rock-forming minerals at temperatures between 297 and 600 K. Physics and
1004 Chemistry of Minerals, 28, 199-210.
1005 Taran, M.N., Langer, K., Abs-Wurmbach, I., Frost, D., and Platonov, A.N. (2004) Local
1006 relaxation around $^{[6]}Cr^{3+}$ in synthetic pyrope-knorringite garnets, $^{[8]}Mg_3{}^{[6]}(Al_{1-x}Cr_x{}^{3+})_2{}^{[4]}Si_3O_{12}$, from electronic absorption spectra. Physics and Chemistry of Minerals,
1008 31, 650-657.
1009 Taran, M. N., Yakovleva, V.V., Vyshnevskyi, O.A., and Panchenko, V.I. (2005) Cr-bearing
1010 beryl - emerald - from Kruta Balka occurrence, western Periazovian area (Ukraine).
1011 Mineralogical Journal (Ukraine) 27, 93-101 (in Ukrainian).

Taran, M.N., Dyar M.D., Khomenko V.M., Joseph S., and Boesenberg, J.S. (2017) Optical absorption, Mössbauer, and FTIR spectroscopic studies of two blue bazzites. Physics and Chemistry of Minerals, 44, 497-507.

Taran, M.N., and Vyshnevskyi, O.A. (2019) Be, Fe^{2+}-substitution in natural beryl: an optical absorption spectroscopy study. Physics and Chemistry of Minerals, https://doi.org/10.1007/s00269-019-01040-2.

Tretyakova, L.I., and Benavides, K.S. (1987) Mineralogical and spectral-colorimetric study of emeralds from the deposits Chivor and Muzo (Colombia). Zapiski RMO (Proceedings of the Russian Mineralogical Society) 116, 713-718 (in Russian).

Tribovillard, N., Algeo, T.J., Lyons, T., and Riboulleau, A. (2006) Trace metals as paleoredox and paleoproductivity proxies: an update. Chemical Geology 232, 12–32.

Vapnik, Y., and Moroz, I. (2000) Fluid inclusions in emerald from the Jos complex (Central Nigeria). Schweizerische Mineralogische Petrographische Mitteilungen, 80, 117-129.

Vapnik, Y., Sabot, B., and Moroz, I. (2005) Fluid inclusions in Ianapera emerald, Southern Madagascar. Interantional Geology Review, 47, 617-662.

von Goerne, G., Franz, G., and Heinrich, W. (2001) Synthesis of tourmaline solid solutions in the system Na_2O-MgO-Al_2O_3-SiO_2-B_2O_3-H_2O-HCl and the distribution of Na between tourmaline and fluid at 30(to 700 °C/ 200 MPa. Contribution Mineralogy Petrology, 141, 160-173.

von Goerne, G., Franz, G., and van Hinsberg, V. J. (2011) Experimental determination of Na-Ca distribution between tourmaline and fluid in the system CaO-Na_2O-MgO-Al_2O_3-SiO_2-B_2O_3-H_2O. Canadian Mineralogist, 49, 137-152.

Wise, M.A., and Anderson, A. J. (2006) The emerald- and spodumene-bearing quartz veins of the Rist emerald mine, Hiddenite, North Carolina. Canadian Mineralogist, 44, 1529-1541.

Wood, D.L., and Nassau, K. (1968) The characterization of beryl and emerald by visible and infrared absorption spectroscopy. American Mineralogist, 53, 777-800.

Zimmermann, J.L., Giuliani, G., Cheilletz A., and Arboleda, C. (1997). Mineralogical significance of flui in channels of Colombian emeralds: A mass-spectrometric study. International Geology Review 39, 425-437.

Zwaan, J.C., Kanis, J., and Petsch, E. J. (1997) Update on emeralds from the Sandawana mines, Zimbabwe. Gems & Gemology, 33, 80-100.

Figure captions

Fig. 1: Position of the Ukrainian Shield in the East European Platform and its tectonic zones (modified from Claesson et al. 2006). Domains: Volynskyi (North-West); RT, Ros-

Tykichskyi; P, Podilskyi (Dnister-Buh); K, Kirovohradskyi (Inhulskyi); MD, Serednoprydniprovskyi; A, Pryazovskyi. Suture zones: HSZ, Holovanivska; KSZ, Kryvorizka; OSZ, Orikhiv-Pavlohradska. Beryl occurrences: emerald KB = Kruta Balka, heliodor V = Volynske.

Fig. 2: Schematic geological map (**a**) and cross section (**b**) of Kruta Balka pegmatite occurrence. The host rocks of emerald are both, meta-ultramafic to metabasic rocks and metasediments, rich in organic matter.

Fig. 3: 3D-image of pegmatite vein with the sampling locations of emerald crystals #16 and #18; the locality of the KBE sample is not recorded in detail, but from a similar position. Cross-hatched area shows erosion cut of the vein; from Taran et al. (2005), with permission of the Mineralogical Journal, Ukraine.

Fig. 4: Hand specimen of emerald from Kruta Balka, Ukraine, with abundant muscovite and albite

Fig. 5: Cr and V content (in apfu) of emeralds from Kruta Balka; shown are the average compositions (large open circles) of three crystals and the individual point analyses (small dots), to illustrate the strong heterogeneity within a crystal and from crystal to crystal. Many crystals from emerald occurrences worldwide show such heterogeneity; two examples are given for the Mananjary deposit, Madagascar (squares; sample 81-193, four crystals; Table EA 1), which is characterized by a large amount of Cr, and for the Sandagawa deposit, Zambia (diamonds; Zwaan et al. 1997), characterized by intermediate Cr and V contents. Note different scales of Cr and V; Cr is generally more abundant.

Fig. 6: Element mapping of crystal KB-1, Kruta Balka; orientation of the crystal's **c**-axis is indicated in corresponding BSE image. Al and Mg are inversely correlated, Mg and Cr (and V, Fe; hardly visible because of low concentrations) are positively correlated. Cr is also enriched in biotite (Bt), in late stage chlorite (Chl), and in muscovite (Ms) intergrown with biotite, but not in large muscovite inclusions. Cr distribution in emerald is indicative of oscillatory zoning and of replacement structures (note Cr-Mg-poor dark areas in center of Cr- and Mg-image). Na is completely independent of other element concentrations, enriched in an irregular network of µm-sized veins; some veins are oriented subparallel and -perpendicular to **c**. Sc, a trace element often observed in beryl, is enriched in apatite (Ap). For further discussion see

text.

Fig. 7: Element mapping of inclusion-free crystal KB-2, Kruta Balka; orientation of the crystal's *c*-axis (and growth direction), traces of prism face *(hki0)* and basal pinakoid *(0001)* are indicated in corresponding BSE image. Al and Cr are inversely correlated, and Mg and Sc (and Fe; hardly visible because of low concentration) are inversely correlated. The zigzag pattern of Mg distribution in the internal part of the crystal indicates sector zoning (see dashed lines) with the **c**-sector enriched in Mg, the **a**-sector enriched in Sc. Oscillatory Cr zoning indicates general preferential Cr incorporation perpendicular to the **c**-axis; arrows in Cr-map point to irregularities in zoning on prism and pinakoid. Na is positively correlated with Mg, but enriched along cracks oriented subparallel and perpendicular to **c** (indicated by arrows). For further discussion see text.

Fig. 8: BSE images of the Kruta Balka emeralds (**a** #16, **c-h** #18). Abbreviations: Brl beryl, Bt biotite, Ms muscovite, Tour tourmaline, Zrn zircon. Zircon inclusions have up to 11 wt% HfO_2, tourmaline is Li-bearing with a calculated content of 0.39 wt% Li_2O corresponding to 0.259 Li apfu.

Fig. 9: (**a**) Polarized optical absorption spectrum of emerald from Kruta Balka, sample #18 (**b**) Optical diffuse reflectance spectrum of sample #16; from Taran et al. (2005), with permission of the Mineralogical Journal, Ukraine.

Fig. 10: Polarized FTIR spectra of emerald from Kruta Balka, sample KBE (**a**) range 6000 to 1500 cm^{-1}; (**b**) detailed area with fundamental H_2O-stretching bands; (**c**) middle IR-part with bands of H_2O-bending vibration; (**d**) CO_2 asymmetric stretching band (comparatively strong for beryls)

Fig. 11: Comparison of measured BeO contents (wt%) with the calculated BeO contents from EPMA, assuming 3.000 Be pfu, for emerald crystals from different localities; + data from Aurisicchio et al. (1988) for emeralds and beryl from emerald localities, photometric determination of BeO (localities in italics); **x** Aurisicchio et al. (1988) for synthetic flux grown beryl. For most samples the calculated BeO content is slightly overestimated, indicating a small amount of substitution of Be. The vertical error bar is 1% relative for BeO measured by SIMS and the horizontal error bar is for 0.26% relative for SiO_2 measured by EPMA and used to calculate BeO, whence the major impact of the SiO_2 measurement on calculated BeO content.

Fig. 12: SiO_2 contents (wt%) of emeralds from localities worldwide determined by EPMA, compared to the calculated BeO content, assuming 3.000 Be pfu (Table 5). Included are also the data for ideal compositions (diamonds), anhydrous beryl (labeled *ideal*) and beryl with a maximum content of 3.2 wt% H_2O (labeled *hydrous*), beryl with octahedral Al = Li + 2Na substitution (labeled *ideal Al-Li*), hydrous femag beryls with 0.5 Al = 0.5 Na + 0.5 Mg and 0.5 Al = 0.5 Na + 0.5 Fe (labeled *ideal hydrous Mg, ideal hydrous Fe*), connected by the dashed line; the tetrahedral substitution Be = Li + Na (labeled *ideal Be-Li*) produces beryl with 65.79 wt% SiO_2, 11.41 wt% BeO (indicated by the arrow) and pezzotaite has the lowest BeO-content with 10.26 wt%. The reference data from pure pegmatitic beryl (open circles, rim and core analysis) lie close to the line and underline the general validity of the assumption 3.000 Be pfu. Average analysis from Kruta Balka emeralds (# 16, 18 and KBE), Manyara (Tanzania), and Mavis Lake (Canada) lie above the line, indicating overestimation of the calculated BeO content by approximately 0.3 wt%. Data from Norway and the Egyptian localities Zabar, Sikait, and Um Kabu below the line; all these analyses show high Si between 6.042 and 6.081 apfu. For further discussion see text.

Fig. 13: Characterization of emerald deposits, based on Cr# = Cr/(Cr+V) vs. Mg# = Mg/(Mg+Fe). Many emerald deposits (24 out of 52) are characterized by high ratios between 0.8 and 0.9, which is the *ultramafic* schist type occurrence, where Cr as the coloring element is predominant, originating from metamorphosed mafic-ultramafic rocks. A small group (11 localities) is considered as *transitional*, where the source for Mg+Fe+Cr+V are both mafic-ultramafic rocks and metasediments; Kruta Balka is a typical example for this group, and most of the Australian deposits belong to this group. All other localities (17) are considered as *sedimentary* with regard to their origin of highly variable Cr# and Mg#. The Cordilleran-type occurrences from Colombia and Canada (Yukon, McKenzie Mts., Lened) are typical examples, but also the Chinese deposits Davdar and Dyaku, Binntal (Switzerland), Pakistan (Sharbag-Swat, Gandao).

Fig. 14: Sum of trivalent (Al+Cr+V+Sc) and divalent cations (Mg+Fe+Mn; in apfu) of emeralds. All analyses are calculated with $Fe_{tot} = Fe^{2+}$ and on the basis of 3.000 Be apfu. The dotted vertical line separates localities with a low amount of substitution from those with a high amount, arbitrarily set at 0.25 apfu; the Ukrainian Kruta Balka occurrence belongs to the group with a low amount of substitution, as most of the deposits classified as transitional and sedimentary. The majority of the 'ultramafic' deposits show a high amount of femag-

component. Exchange vectors are shown in the inset lower left; the dashed line indicates the effect of the ideal femag substitution ^{VI}(Al,Cr,V,Sc) = ^{VI}(Mg, Fe_{tot}^{2+},Mn) + ^{channel}(Na,K,Cs), which goes up to 0.5 Mg+Fe+Mn, which is considered as the actual end-member. For further discussion see text.

Fig. 15: Sum of divalent cations (Mg, Fe^{2+}, Mn) and monovalent cations (Na, K, Rb, Cs) of emeralds' EPMA from Kruta Balka, compared to analyses from the literature and from our data base (for data base and references see Table 5). The dashed line indicates the effect of the ideal femag substitution ^{VI}(Al,Cr,V,Sc) = ^{VI}(Mg, Fe_{tot}^{2+},Mn) + ^{channel}(Na,K,Cs). The Kruta Balka emeralds are exceptional showing a high amount of the substitution ^{VI}(Al,Cr,V,Sc) = ^{VI}(Li) + 2 ^{channel}(Na,K,Cs); other data points below the line include emerald from Dyaku, China, Mavis Lake, Canada, Binntal, Switzerland, from Crabtree Mts, USA (Wise and Anderson, 2006), which also show a significant amount of Li. The emeralds from Sandawana/Tanzania are the only ones, which reach 0.5 apfu for both parameters. Data points above the line indicate the presence of some Fe^{3+}; open diamonds connected with a dotted line indicate analyses where Fe_{tot} is assumed to be all Fe^{3+}, and which stll plot significantly above the line, indicating a different substitution. For further discussion see text.

Deposit items

List of Tables for Electronic Appendix EA

Table EA 1: Geological origin and preliminary characterization of emerald samples for comparison by means of SIMS (Li, Be determination, see Table 2; in bold) and EPMA; Li_2O contents were determined by spectrometry, H_2O contents by coulorimetry; c = core; r = rim

Table EA 2: Method of Li-Be determination with SIMS (GFZ Potsdam)

Table EA 3: a) Point analyses of Kruta Balka emeralds and b-f) analysis of inclusions

Table EA 4: EPMA of emeralds from different localities worldwide, this study

Table EA 5: Details of XRD Rietveld parameters for refinement

Table EA 6: Average *typical* EPMA of emerald from localities worldwide, and calculated formulae.

Tables

Table 1: Major substitutions in emerald with pure beryl $Al_2Be_3[Si_6O_{18}]$ as additive component

sites involved	exchange vector	channel 2a (ch)	channel 2b (ch)	octahedral Al (oct)	tetrahedral Be (tet)	
ch	$H_2O\square_{-1}$	H_2O				*hydrous beryl*
oct	$CrAl_{-1}$			Cr		*'emerald'*
	VAl_{-1}			V		
	$ScAl_{-1}$			Sc		bazzite
	$Fe^{3+}Al_{-1}$			Fe^{3+}		stoppaniite
ch-oct	$Na(Mg,Fe^{2+})\square_{-1}Al_{-1}$		Na	Mg,Fe^{2+}		*'femag-beryl'*
ch-tet	$NaLi\square_{-1}Be_{-1}$		Na		Li	avdeevite
	$CsLi\square_{-1}Be_{-1}$	Cs			Li	pezzotaite
ch-oct	$Na_2Li\square_{-2}Al$		Na	Li		
oct-tet	$MgBe_{-1}$			Mg	Al	*'Be-cordierite' (synthetic)*

Note: Names not approved by the International Mineralogical Association are italicized.

Table 2: Results of SIMS determination of BeO and Li_2O of emeralds, calculated BeO contents on the basis of EMP analyses assuming 3.000 Be pfu and Li_2O-determination by photometry

Sample	Locality	BeO wt% (SIMS)		BeO wt% (calc)		Li_2O wt% (SIMS)		Li_2O wt% (photometry)	
		core	rim	core	rim	core	rim	core	rim
78-14	Ural Mountains, Russia	13.55	13.64	13.68	13.70	0.20	0.21	0.274	0.32
78-16	Leydendorp, Transvaal	12.71	12.73	12.87	12.81	0.077	0.053	na	
78-40	West Australia	13.22	13.11	13.13	13.17	0.078	0.065	na	
78-78	Takowaja, Ural Mountains, Russia	13.58; 13.9(c-r)	13.906	13.10	13.17	0.26; 0.28(c-r)	0.403	0.215	
78-83	Mouzo, Colombia	13.56	13.40	13.85	13.92	0.011	0.013	na	
80-47	Habachtal, Austria	13.24	13.21	13.49	13.52	0.020	0.067	na	
80-51	Habachtal, Austria	13.09; 13.10(c-r)	12.81	13.42		0.015; 0.019(c-r)	0.027	na	

c-r transitional core to rim; na not analyzed

Table 3: EPMA data from emeralds from Kruta Balka, Ukraine; Li_2O by photometry from Rozanov and Lavrinenko (1979)

Sample #	**#16**	**#18**	**KBE**	**average**	**corrected[2]**
n[1]	15	10	4		
SiO_2 wt%	64.81	65.10	63.77	64.56	
TiO_2	0.01	0.01	n.d.	0.01	
Al_2O_3	17.62	17.57	16.84	17.34	
Cr_2O_3	0.15	0.15	0.31	0.20	
V_2O_3	0.07	0.06	0.01	0.05	
FeO_{tot}	0.20	0.18	0.30	0.23	
MnO	0.02	0.05	n.d.	0.04	
MgO	0.35	0.35	0.67	0.46	
CaO	0.02	0.03	n.d.	0.02	
Na_2O	1.76	1.89	1.81	1.82	
K_2O	0.03	0.01	0.05	0.03	
Li_2O	0.41	0.41	0.41	0.41	
Cs_2O	0.55	0.41	0.61	0.52	
BeO_{calc}	13.61	13.66	13.45	13.62	13.32
H_2O					1.50
sum	99.62	99.89	98.22	99.31	100.51
apfu					
Si	5.913	5.918	5.917	5.915	5.937
Ti	0.001	0.001	0.000	0.001	0.001
Al	1.893	1.882	1.841	1.873	1.878
Cr	0.011	0.010	0.022	0.015	0.015
V	0.005	0.005	0.000	0.003	0.004
Fe^{2+}_{tot}	0.015	0.014	0.023	0.018	0.018
Mn	0.002	0.004	0.000	0.003	0.003
Mg	0.048	0.048	0.093	0.063	0.063
Ca	0.002	0.003	0.000	0.002	0.002
Na	0.311	0.332	0.325	0.323	0.324
K	0.004	0.002	0.006	0.004	0.004
Li	0.150	0.149	0.152	0.150	0.152
Cs	0.022	0.016	0.024	0.018	0.020
Be	3.000	3.000	3.000	3.000	2.944
H_2O					0.920

1) n = number of point analyses; 2) calculated BeO contents are corrected by deducting 0.3 wt% from the average BeO content calculated for 3.000 Be per formula unit

Table 4: Cation coefficients and cation distribution of emeralds of this study (BeO and Li_2O determined by SIMS) and from Aurisicchio et al. (1988; labeled as 'Auris'), based on 18 oxygen, arranged with increasing octahedral substitution

Sample No.	Locality	Channel			Octahedra							Be tetrahedra			Si tetrahedra		
		Na (+K)	Cs	Li	Al	Mg	Fe^{2+} (+Mn)	Cr	V	Li	Σ VI (+Ca)	Be	Li	Si/Al	Si	Al	Be
78-83c	Colombia	0.061	-	-	1.915	0.041	0.004	0.005	0.004	-	1.987	2.918	0.005	0.002/0.075	6.000	-	-
78-83r	Colombia	0.062	0.001	-	1.911	0.038	0.010	0.006	0.001	-	1.966	2.935	0.004	0.031/0.030	6.000	-	-
10 Auris	Muzo	0.088			1.780	0.120	0.024	0.027	0.047	-	1.998	2.961	-	0.024/0.014	6.000	-	-
78-78c	Ural Mts.	0.100	0.002	**0.092**	1.906	0.069	0.011	0.004	0.001	**0.013**	2.001	3.000	-	-	**5.942**	**0.027**	**0.03**
78-78r	Ural Mts.	0.097	0.002	**0.104**	1.916	0.059	0.012	0.002	0.001	-	2.000	3.000	-	-	**5.925**	**-**	**0.08**
78-14c	Ural Mts.	0.132	0.002	**0.032**	1.932	0.036	0.008	0.001	0.000	**0.044**	2.000	2.998	0.002	-	**5.977**	**0.023**	-
78-14r	Ural Mts.	0.118	0.002	**0.027**	1.921	0.045	0.013	-	-	**0.021**	2.000	2.975	0.025	-	**5.985**	**0.015**	-
26 Auris	Ural Mts.	0.091	-	**0.019**	1.924	0.060	0.019	-	-	-	2.003	2.979	0.020	0.001/-	6.000		
78-40c	Westaustralia	0.096	-	-	1.865	0.075	0.025	0.007	0.001	-	1.977	2.893	0.024	0.016/0.066	6.000	-	-
78-40r	Westaustralia	0.100	0.001	-	1.853	0.122	0.047	0.034	0.001	-	1.990	2.913	0.029	0.011/0.047	6.000	-	-
9 Auris	Brazil	0.340	-	-	1.800	0.158	0.039	-	-	-	1.997	**2.870**	**0.037**	0.008/**0.085**	6.000		
24 Auris	Mocambique	0.243	-	-	1.680	0.258	0.063	-	-	-	2.001	2.900	0.015	0.008/	6.000		
78-16c	South Africa	0.179	0.012	-	1.681	0.249	0.074	0.007	0.002	-	2.025	2.903	0.025	0.042/0.030	6.000	-	-
78-16r	South Africa	0.251	0.010	-	1.652	0.257	0.076	0.008	0.001	-	1.995	2.900	0.025	0.037/0.039	6.000		
23 Auris	Austria	0.316	-	-	1.623	0.321	0.030	0.026	-	-	2.000	2.960	0.015	0.025/	6.000		
80-47c	Austria	0.369	0.001	-	1.596	0.342	0.049	0.002	0.001	-	1.995	2.953	0.007	0.006/0.034	6.000	-	-
80-47r	Austria	0.397	0.001	-	1.611	0.354	0.045	0.000	0.002	-	2.006	2.965	0.025	-/0.010	**5.970**	**0.030**	-
80-51c	Austria	0.417	0.001	-	1.528	0.381	0.071	0.024	0.002	-	1.982	2.929	0.008	0.006/0.057	6.000	-	-
80-51r	Austria	0.404	0.002	-	1.524	0.371	0.070	0.023	0.002	-	1.991	2.931	0.007	0.008/0.054	6.000	-	-
4 Auris	Pakistan	0.344	-	-	1.468	0.362	0.096	0.072	-	-	1.998	2.908	0.011	**0.049**/0.032	6.000		

Note: Extreme values are marked in bold. $Fe_{tot} = Fe^{2+}$; traces of Rb, Sc, and Ti have been neglected; traces of Mn have been added to Fe, of K to Na, of Ca to sum of octahedral cations; c = core, r = rim.

Table 5: Summary of emerald EPMA data from localities worldwide; listed are wt% SiO_2 and wt% BeO, calculated for 3.000 Be apfu, and other critical parameters in apfu for classification and characterization of emeralds. For complete analyses and calculated formulae see Table EA 6.

Country	**Afghanistan**	**Australia**	**Australia**	**Australia**	**Australia**	**Austria**	**Brazil**	**Brazil**	**Brazil**	**Brazil**
Locality	**Panjsher**	**Emmaville**	**Poona**	**Menzies**	**West. Aust**	**Habachtal**	**Bahia**	**Salinhina**	**Carnaíba**	**Fazenda Bomfin**
SiO_2 (wt%)	66.59	66.94	65.78	64.98	65.55	64.09	66.77	65.21	64.08	64.75
BeO (wt%)	13.84	13.95	13.70	13.54	13.69	13.36	13.87	13.51	13.33	13.50
Al+Sc+Cr+V	1.833	1.994	1.919	1.834	1.920	1.621	1.852	1.523	1.717	1.661
Mg+Fe+Mn	0.175	0.020	0.069	0.170	0.11	0.386	0.131	0.479	0.289	0.360
Na+K+Rb+Cs	0.134	0.011	0.081	0.172	0.10	0.358	0.131	0.363	0.200	0.329
Mg#	0.71	0.23	0.73	0.70	0.67	0.89	0.71	0.90	0.85	0.86
Cr#	0.89	0.87	0.73	0.88	0.93	0.95	0.72	0.03	0.95	0.95
references	Groat et al. 2008 Aurisicchio et al. 2018	Loughrey et al. 2012	Morteani& Rhede Aurisicchio et al. 2018	Schwarz 1991	this study sample 78-40	Franz et al. 1986 Aurisicchio et al. 2018 this study	Schwarz 1990	Schwarz 1990	Eidt & Schwarz 1988 Aurisicchio. et al. 2018	Santiago et al. 2018

Table 5 ctd.

Brazil	**Brazil**	**Brazil**	**Brazil**	**Bulgaria**	**Canada**	**Canada**	**Canada**	**Canada**	**Canada**
Itabira Belmont	**St Terezinha**	**Socotó**	**Tauá**	**Rila**	**Tsa da Glisza**	**Yukon**	**Mavis Lake**	**Lened**	**McKenzie Mts**
66.28	66.59	64.98	65.12	64.37	64.40	64.24	63.58	65.17	63.67
13.86	13.84	13.62	13.62	13.42	13.41	13.37	13.41	13.62	13.28
1.862	1.539	1.758	1.645	1.769	1.808	1.792	1.925	1.888	1.756
0.198	0.481	0.352	0.423	0.196	0.198	0.215	0.109	0.145	0.270
0.124	0.325	0.197	0.326	0.189	0.186	0.195	0.215	0.147	0.237
0.80	0.80	0.84	0.81	0.82	0.81	0.95	0.74	0.81	0.79
0.90	0.95		0.94	1.00	0.95	0.95	0.92	0.00	0.03
Hänni et al. 1987	Schwarz 1990 Groat et al. 2008	Schwarz et al. 1988a, 1990	Schwarz et al. 1988b	Groat et al. 2008	Groat et al. 2002	Groat et al. 2002	Brand et al. 2009	Lake et al. 2017 Marshall et al. 2004	Hewton et al. 2013

Table 5 ctd.

China Davdar	China Dyaku	Colombia Muzo, Chivor	Egypt Zabara	Egypt Um Kabu	Egypt Sikait	Ethiopia Kenticha	India Raigsh	Kazachstan Delbegetey	Madagascar Ianapera	Madagascar Mananjary
65.98	63.31	66.61	65.90	65.39	66.26	64.97	66.15	65.99	63.97	63.04
13.7	13.25	13.78	13.64	13.43	13.65	13.53	13.71	13.83	13.34	13.10
1.848	1.867	1.840	1.489	1.516	1.576	1.669	1.624	2.000	1.577	1.580
0.142	0.165	0.110	0.484	0.425	0.355	0.332	0.343	0.026	0.501	0.448
0.113	0.202	0.107	0.192	0.274	0.150	0.302	0.301	0.004	0.156	0.249
0.91	0.84	0.91	0.88	0.83	0.89	0.818	0.88	0.26	0.80	0.75
0.32	0.12	0.55	1.00	1.00	1.00	0.928	1.00	0.80	0.93	0.98
Marshal et al. 2012	Marshal pers comm	Groat et al. 2008 Aurisicchio. et al. 2018 Pignatelli et al. 2015	Aurisicchio. et al. 2018	Grundmann & Morteani 2008 Groat et al. 2008	Grundmann & Morteani 2008 Aurisicchio et al. 2018 Groat et al. 2008	Aurisicchio. et al. 2018 Marshall unpub	Aurisicchio. et al. 2018	Groat et al. 2008 .	Groat et al. 2008 Vapnik et al. 2005	Aurisicchio. et al. 2018 Vapnik et al. 2006 this study

Table 5 ctd.

Mocambique Morrua	Namibia Maltahöhe	Nigeria Jos	Norway Bryrud/Eidsvoll	Pakistan Khaltaro	Pakistan Charbag-Swat	Pakistan Gandao	Russia Malyshesvk	Russia Mariinskoye	Russia Takowaya
63.84	63.92	66.21	67.23	65.93	63.22	63.17	65.57	63.05	64.11
13.29	13.29	13.83	13.89	13.77	13.18	13.65	13.69	13.25	13.37
1.728	1.566	1.972	1.918	1.861	1.626	1.603	1.865	1.742	1.895
0.306	0.450	0.055	0.022	0.155	0.393	0.420	0.143	0.362	0.081
0.199	0.381	0.040	0.015	0.174	0.373	0.379	0.145	0.238	0.101
0.80	0.82	0.171	0.53	0.78	0.95	0.81	0.82	0.91	0.83
0.89	0.90	0.415	0.13	0.95	0.95	0.30	0.40	0.96	1.00
Aurisicchio. et al. 2018 Aurisicchio et al. 1988 this study	this study	Aurisicchio. et al. 2018 Vapnik & Moroz 2000 Groat et al. 2008	Schwarz 1991 Loughrey et al. 2013	Groat et al. 2008 Laurs et al. 1996	Groat et al. 2008	Groat et al. 2008	Aurisicchio. et al. 2018	Groat et al. 2008	this study

Table 5 ctd.

Spain Franqueira	South Africa Leydsdorp	Switzerland Binntal	Tanzania Sumbawanga	Tanzania Manyara	Ukraine Kruta Balka	USA Crabtree Mts.	Zambia Miku/Kitwe	Zambia Chantete	Zambia Kagem	Zimbabwe Sandawana
66.06	63.61	65.44	66.28	63.50	64.56	64.34	63.43	64.09	62.90	65.05
13.72	13.23	13.66	13.82	13.40	13.62	13.40	13.31	13.32	13.06	13.66
1.753	1.702	1.838	1.968	1.821	1.891	1.794	1.714	1.682	1.635	1.574
0.237	0.325	0.170	0.052	0.334	0.083	0.199	0.326	0.353	0.400	0.465
0.214	0.213	0.215	0.023	0.210	0.345	0.232	0.345	0.222	0.228	0.488
0.81	0.77	0.99	0.41	0.88	0.78	0.87	0.80	0.84	0.81	0.89
0.90	0.83	0.29	0.86	0.00	0.78	0.94	0.92	0.92	0.91	0.96
Martín-Izard et al. 1995 this study	Schwarz et al. 1996 Nwe & Mortani 1983 this study	Marshall et al. 2017	Aurisicchio. et al. 2018	Groat et al. 2008	this study	Wise & Anderson 2006 this study	Aurisicchio. et al. 2018 Groat et al. 2008	Groat et al. 2008	Groat et al. 2008	Aurisicchio. et al. 2018 Zwaan 2006

List of Tables for Electronic Appendix EA

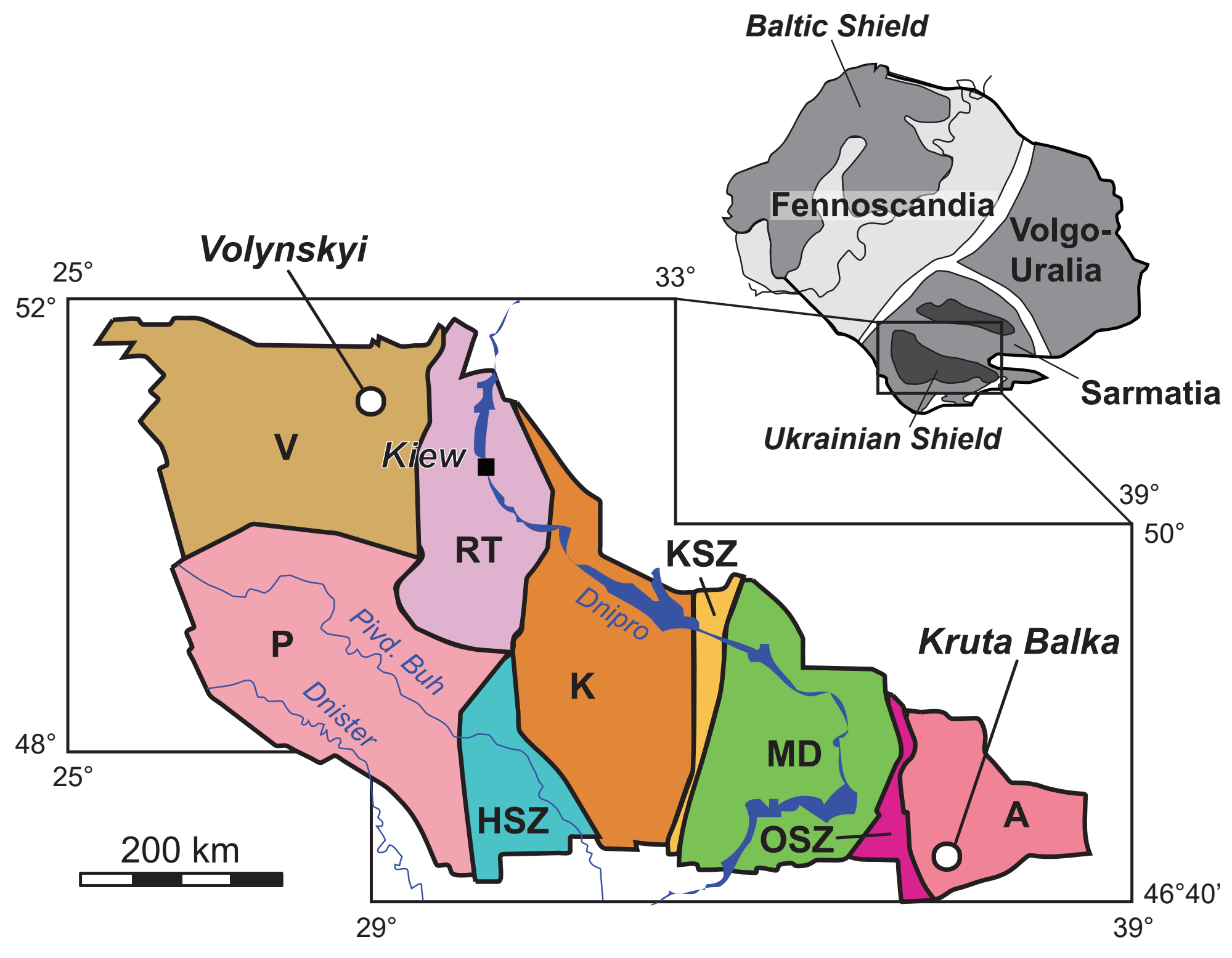
Baltic Shield
Fennoscandia
Volgo-
Uralia
Sarmatia
Ukrainian Shield
Volynskyi
25°
52°
33°
39°
50°
V
Kiew
RT
KSZ
Dnipro
P
Pivd. Buh
Dnister
K
Kruta Balka
MD
HSZ
OSZ
A
48°
25°
200 km
46°40'
29°
39°

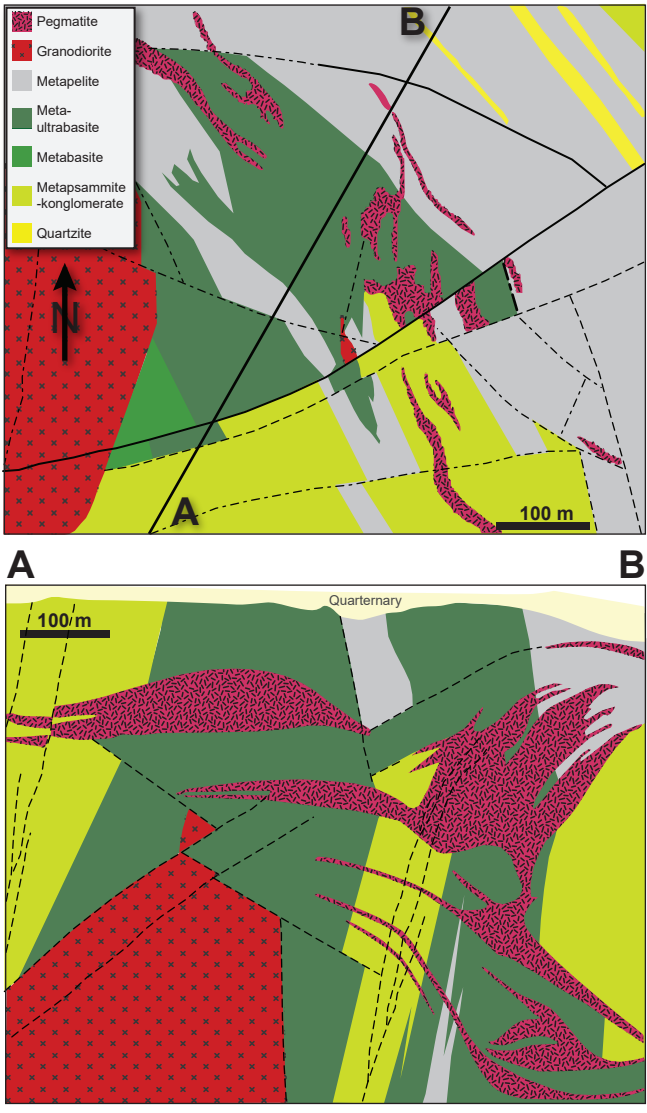
Pegmatite
Granodiorite
Metapelite
Meta-
ultrabasite
Metabasite
Metapsammite
-konglomerate
Quartzite
N
B
A
100 m
A
B
Quarternary
100 m

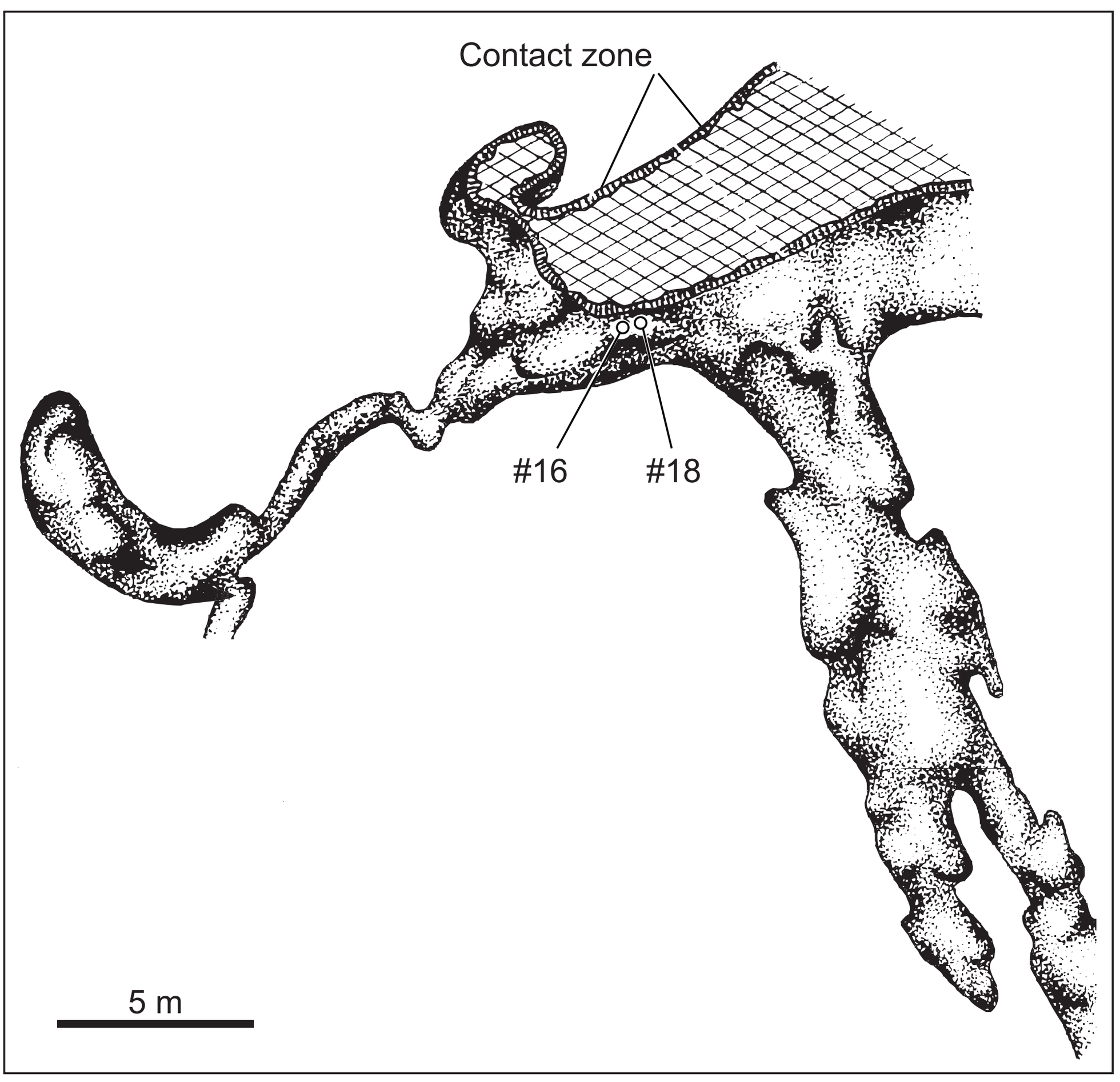
Contact zone
#16
#18
5 m

Fig. 4

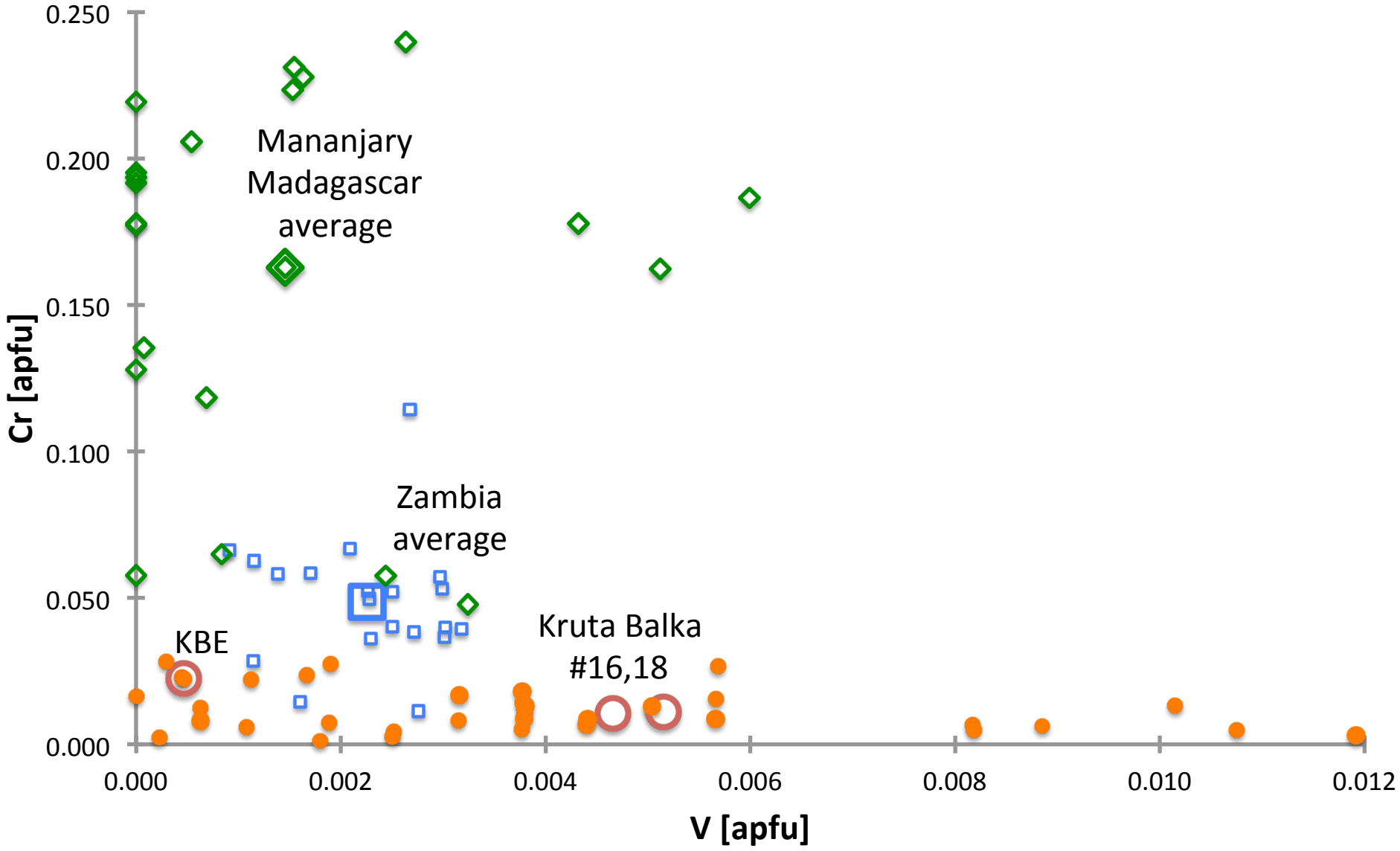
0.250
0.200
0.150
0.100
0.050
0.000
Cr [apfu]
0.000
0.002
0.004
0.006
0.008
0.010
0.012
V [apfu]
Mananjary
Madagascar
average
Zambia
average
KBE
Kruta Balka
#16,18

Fig. 5

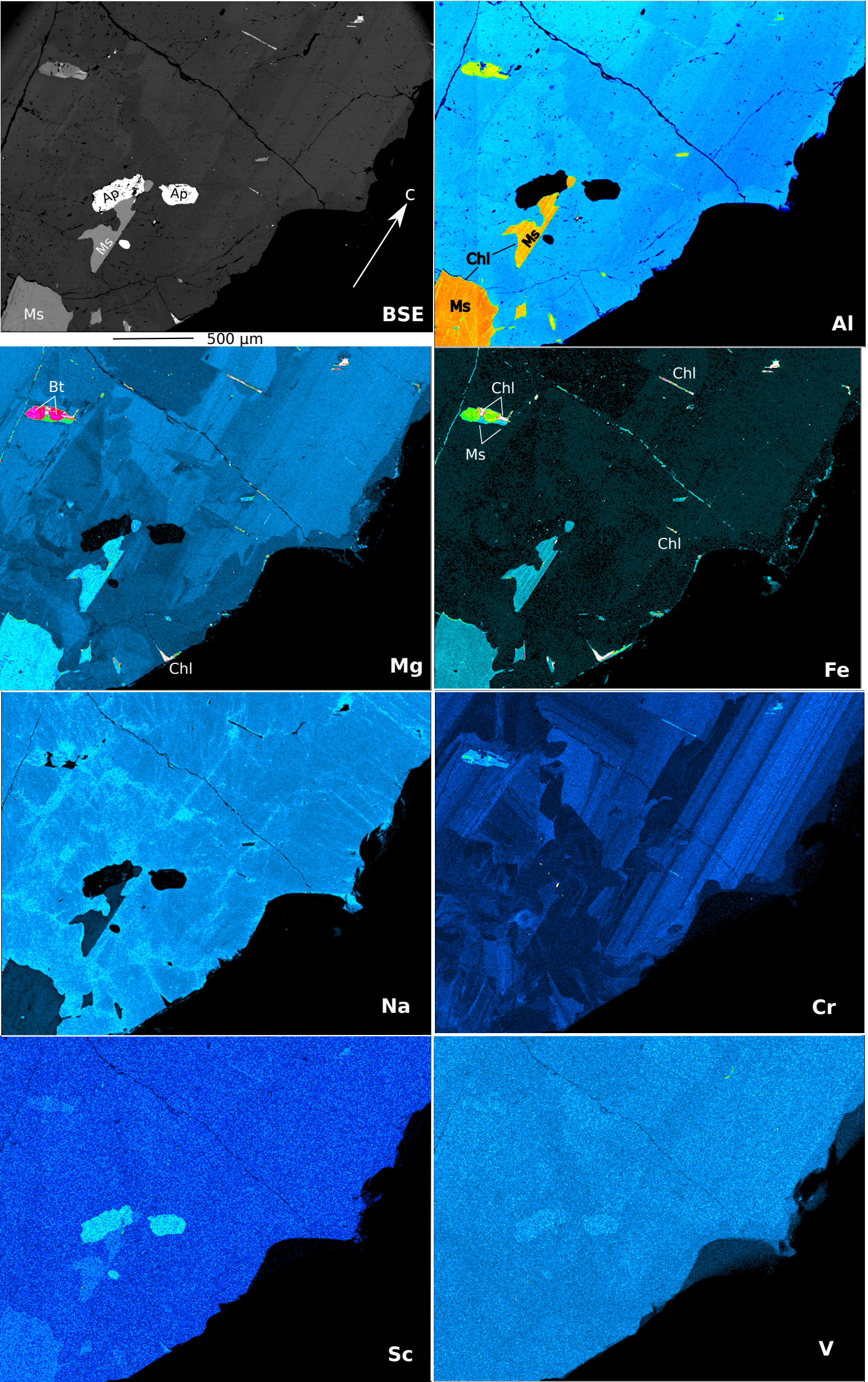
Ap
Ap
Ms
C
Ms
BSE
500 µm
Chl
Ms
Ms
Al
Bt
Chl
Mg
Chl
Ms
Chl
Chl
Fe
Na
Cr
Sc
V

Fig. 6

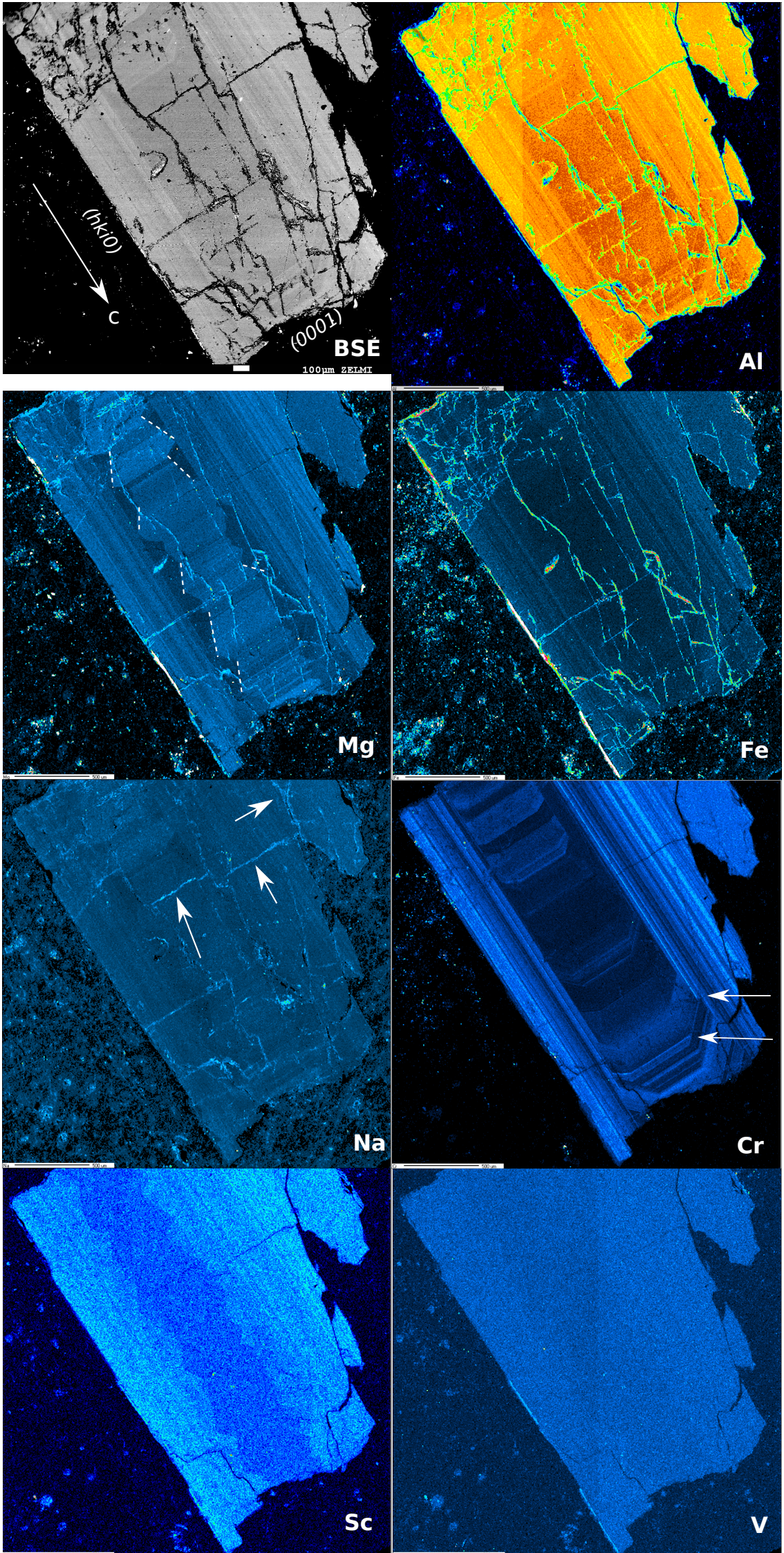

Fig. 7

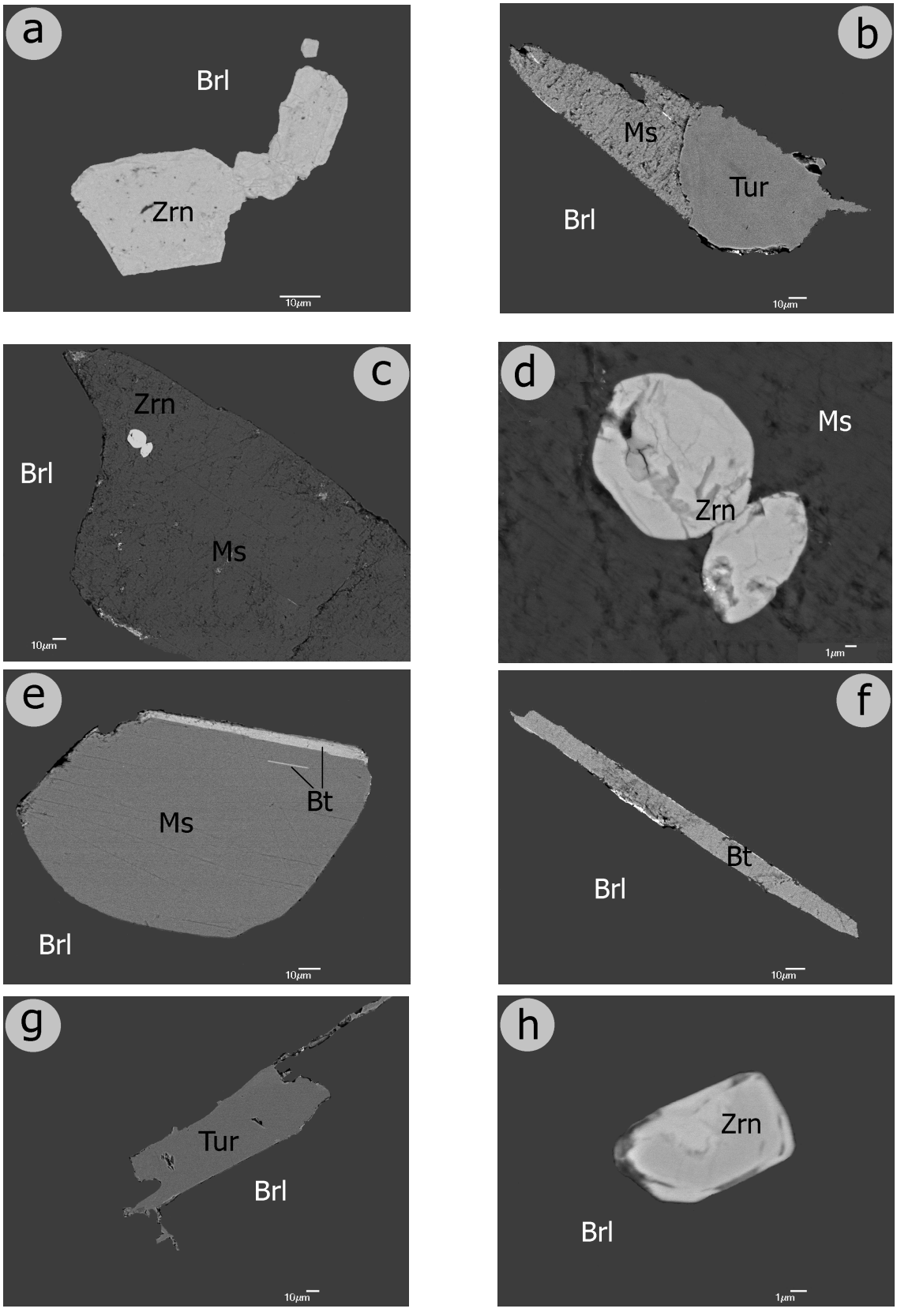
a
Brl
Zrn
10μm
b
Ms
Tur
Brl
10μm
c
Zrn
Brl
Ms
10μm
d
Ms
Zrn
1μm
e
Bt
Ms
Brl
10μm
f
Bt
Brl
10μm
g
Tur
Brl
10μm
h
Zrn
Brl
1μm

Fig. 8

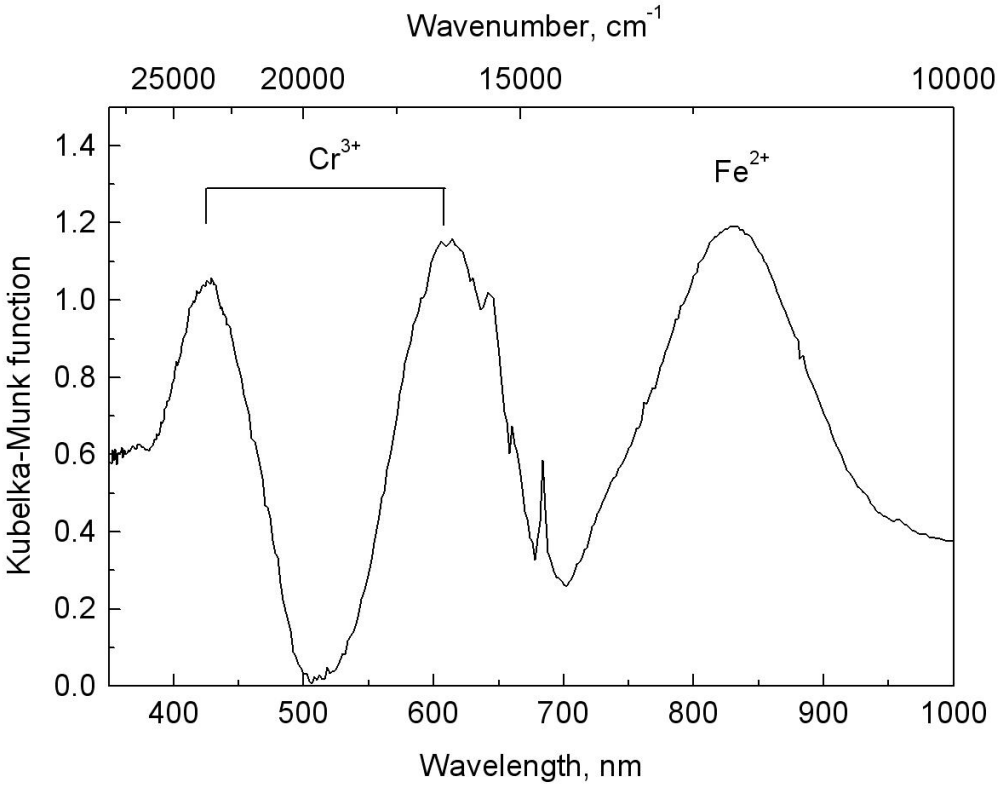
Wavenumber, cm-1
25000
20000
15000
10000
Cr3+
Fe2+
Kubelka-Munk function
1.4
1.2
1.0
0.8
0.6
0.4
0.2
0.0
400
500
600
700
800
900
1000
Wavelength, nm

Fig. 9a

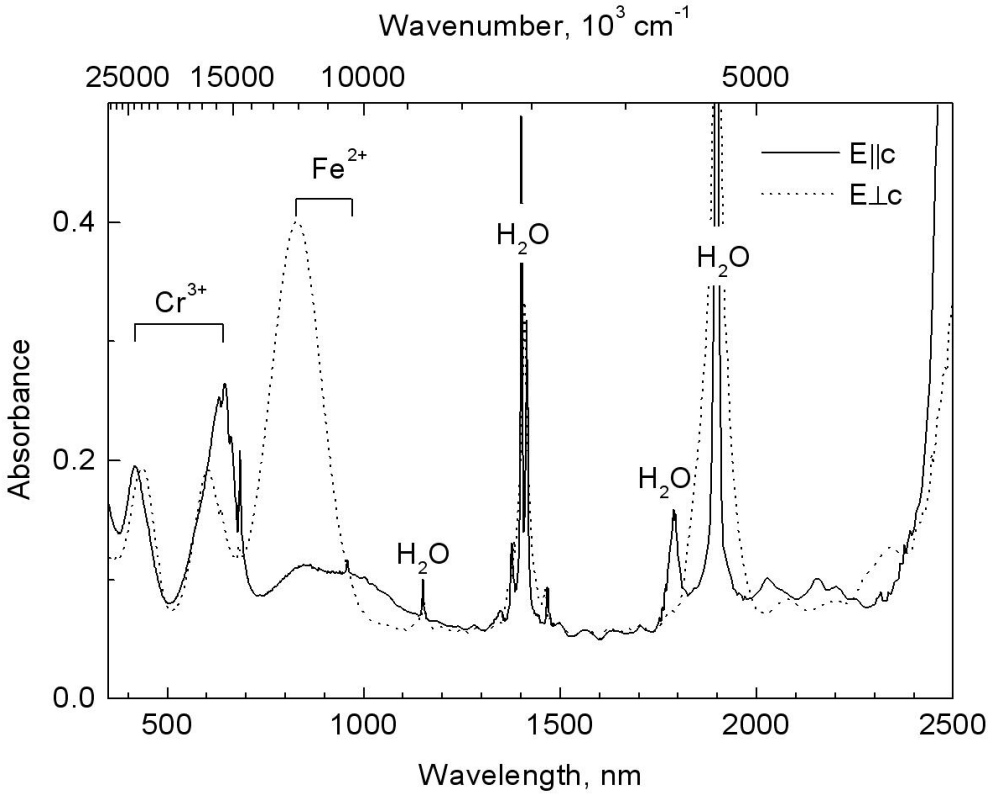
Wavenumber, 10^3 cm-1
25000
15000
10000
5000
E||c
E⊥c
Fe2+
Cr3+
H2O
H2O
H2O
H2O
Absorbance
0.4
0.2
0.0
500
1000
1500
2000
2500
Wavelength, nm

Fig. 9b

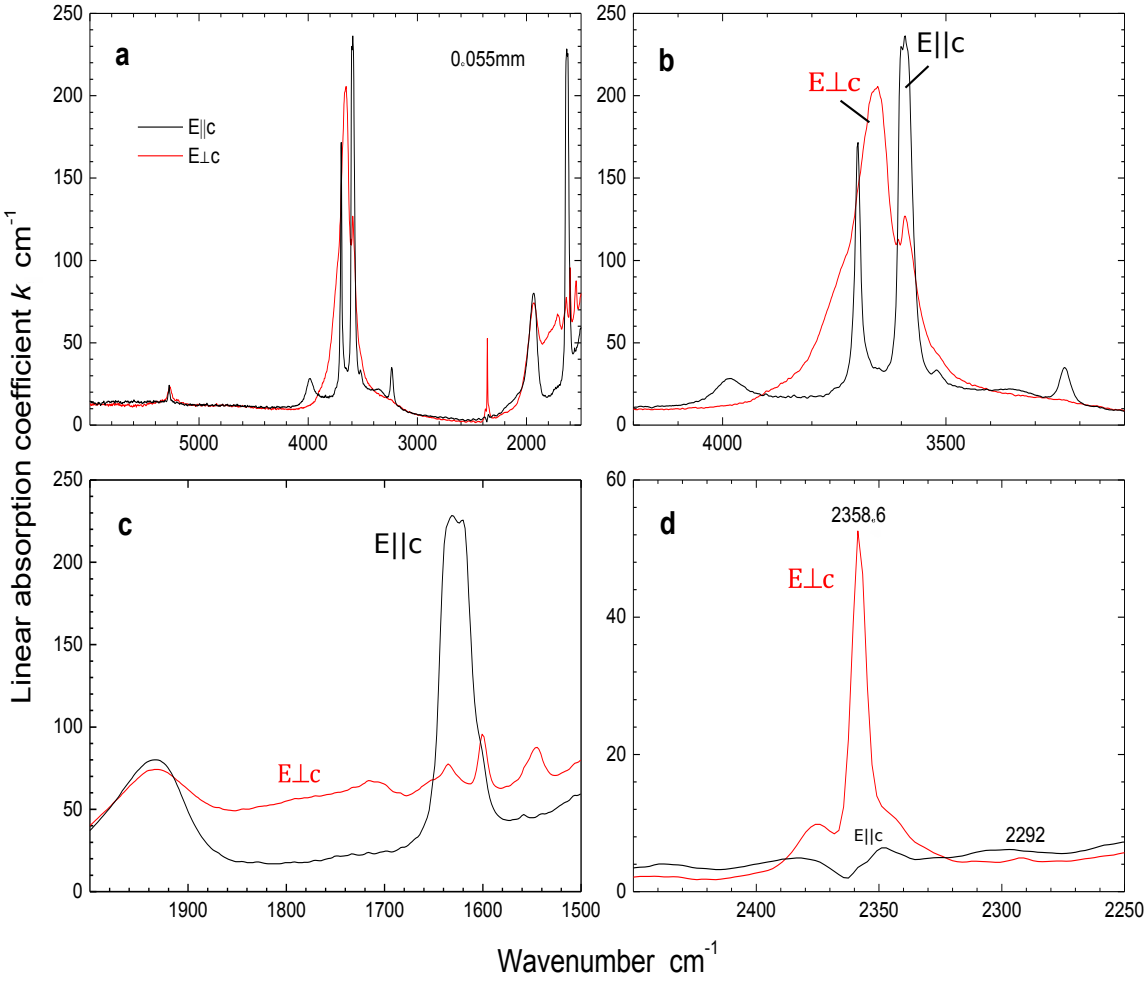
a
0.055mm
E||c
E⊥c
b
E⊥c
E||c
c
E||c
E⊥c
d
2358.6
E⊥c
E||c
2292
Linear absorption coefficient k cm-1
Wavenumber cm-1

Fib. 10

Fig. 11

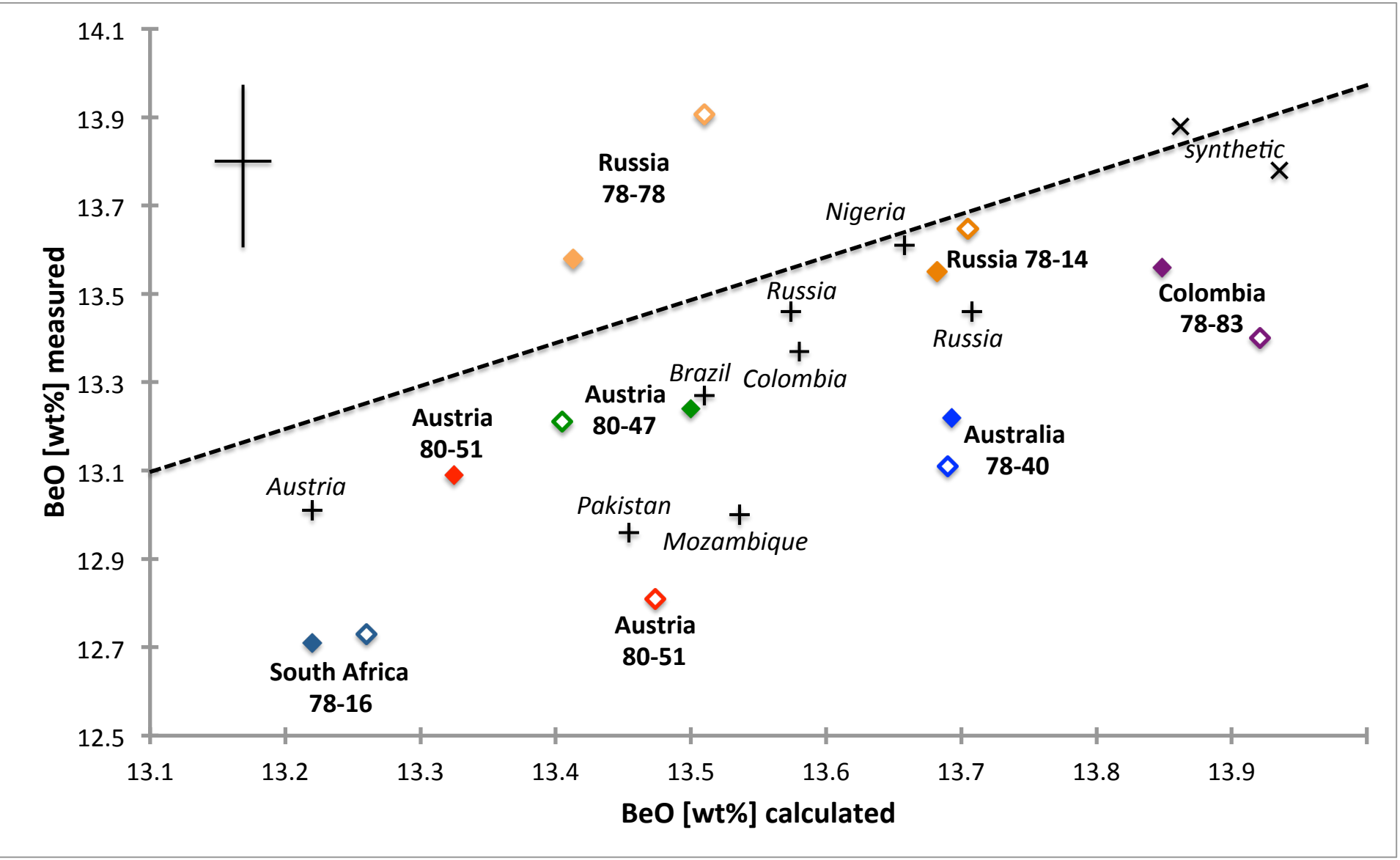
14.1
13.9
13.7
13.5
13.3
13.1
12.9
12.7
12.5
BeO [wt%] measured
13.1
13.2
13.3
13.4
13.5
13.6
13.7
13.8
13.9
BeO [wt%] calculated
Russia
78-78
synthetic
Nigeria
Russia 78-14
Colombia
78-83
Russia
Russia
Brazil
Colombia
Austria
80-47
Austria
80-51
Australia
78-40
Austria
Pakistan
Mozambique
Austria
80-51
South Africa
78-16

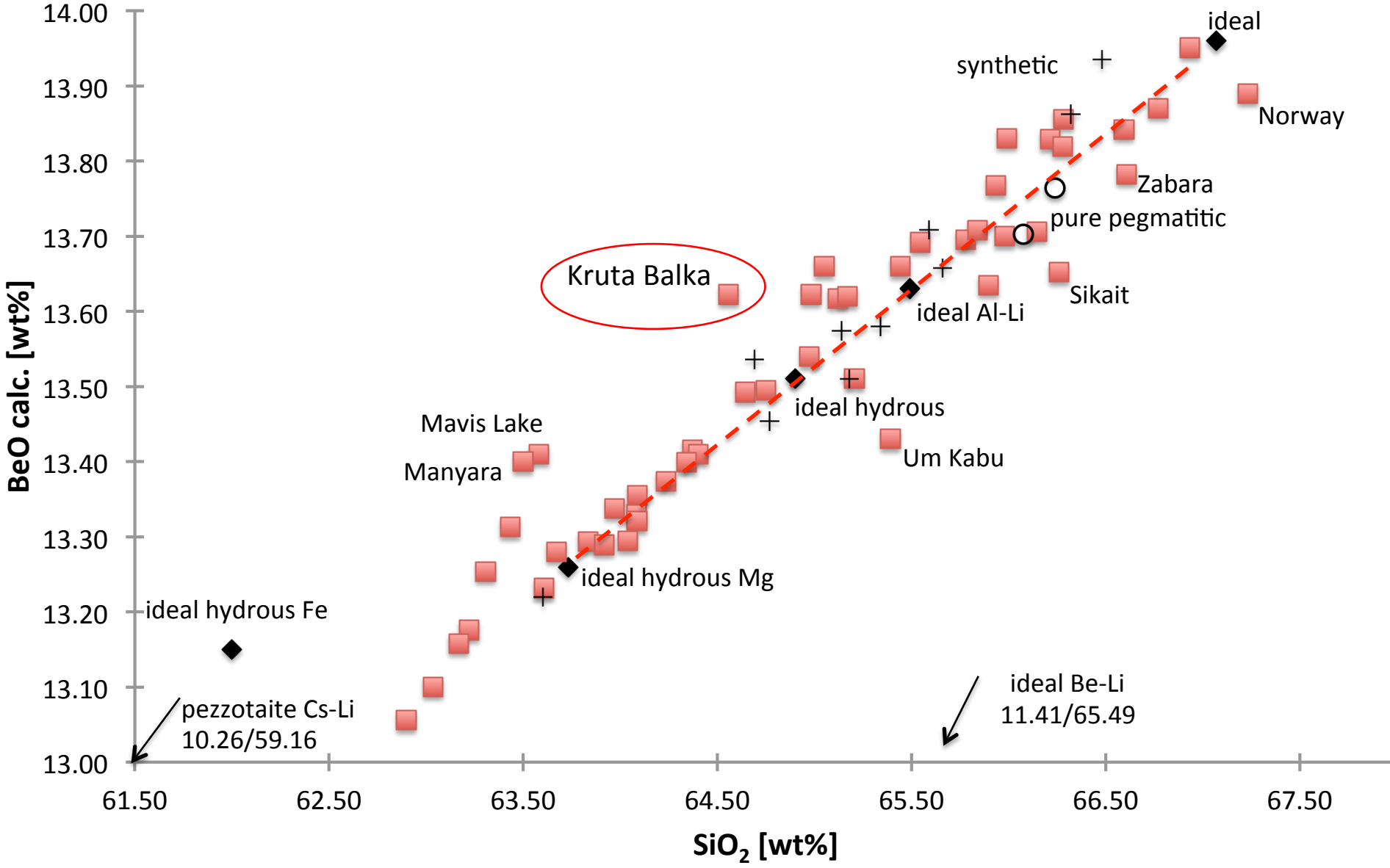
14.00
13.90
13.80
13.70
13.60
13.50
13.40
13.30
13.20
13.10
13.00
BeO calc. [wt%]
61.50
62.50
63.50
64.50
65.50
66.50
67.50
SiO2 [wt%]
ideal
synthetic
Norway
Zabara
pure pegmatitic
Kruta Balka
Sikait
ideal Al-Li
ideal hydrous
Mavis Lake
Manyara
Um Kabu
ideal hydrous Mg
ideal hydrous Fe
pezzotaite Cs-Li
10.26/59.16
ideal Be-Li
11.41/65.49

Fig. 12

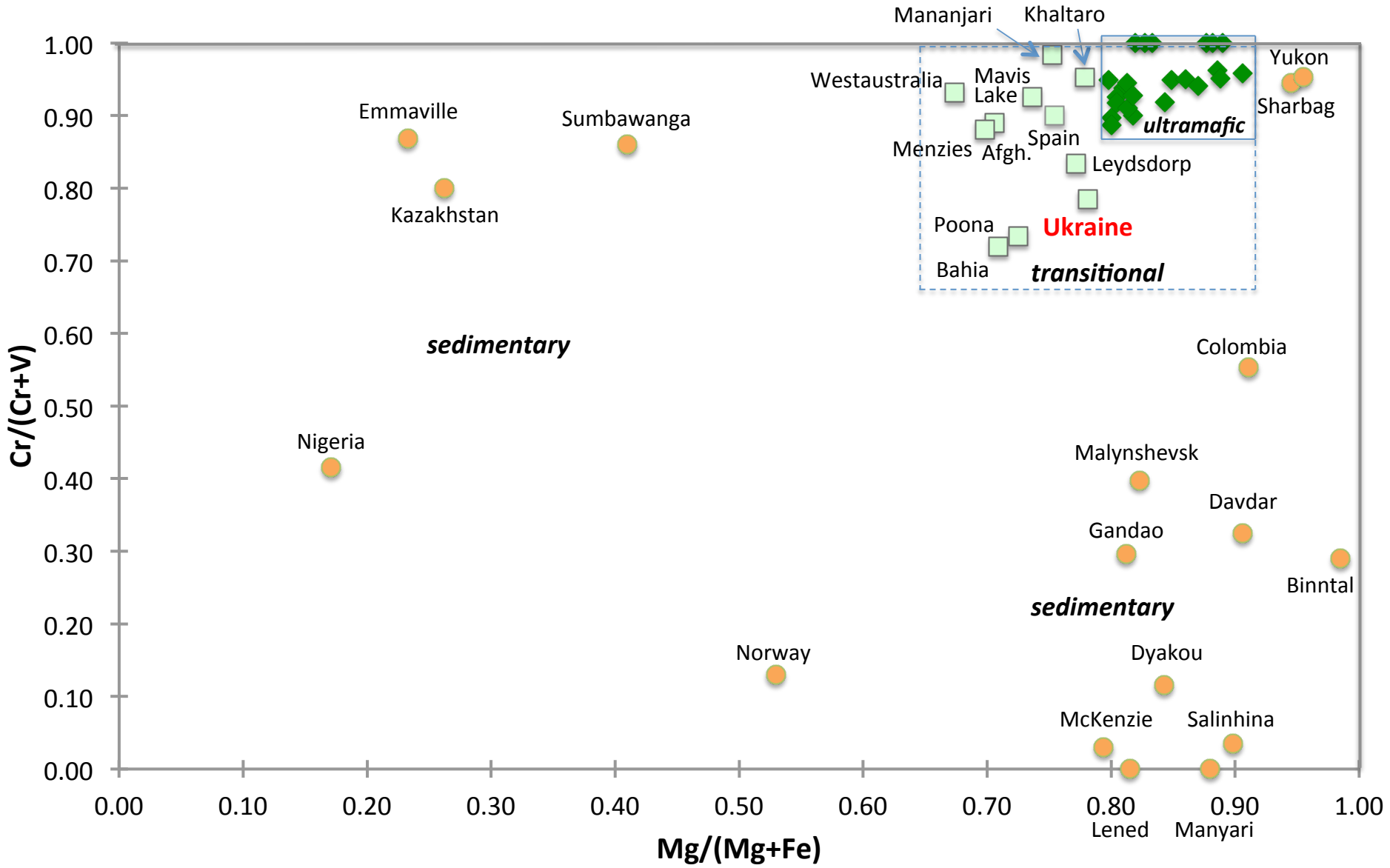
Mananjari
Khaltaro
Yukon
Westaustralia
Mavis
Lake
Sharbag
Emmaville
Sumbawanga
ultramafic
Spain
Menzies
Afgh.
Leydsdorp
Kazakhstan
Poona
Ukraine
Bahia
transitional
Colombia
sedimentary
Nigeria
Malynshevsk
Davdar
Gandao
Binntal
sedimentary
Norway
Dyakou
McKenzie
Salinhina
Lened
Manyari
Cr/(Cr+V)
Mg/(Mg+Fe)
1.00
0.90
0.80
0.70
0.60
0.50
0.40
0.30
0.20
0.10
0.00
0.00
0.10
0.20
0.30
0.40
0.50
0.60
0.70
0.80
0.90
1.00

Fig. 13

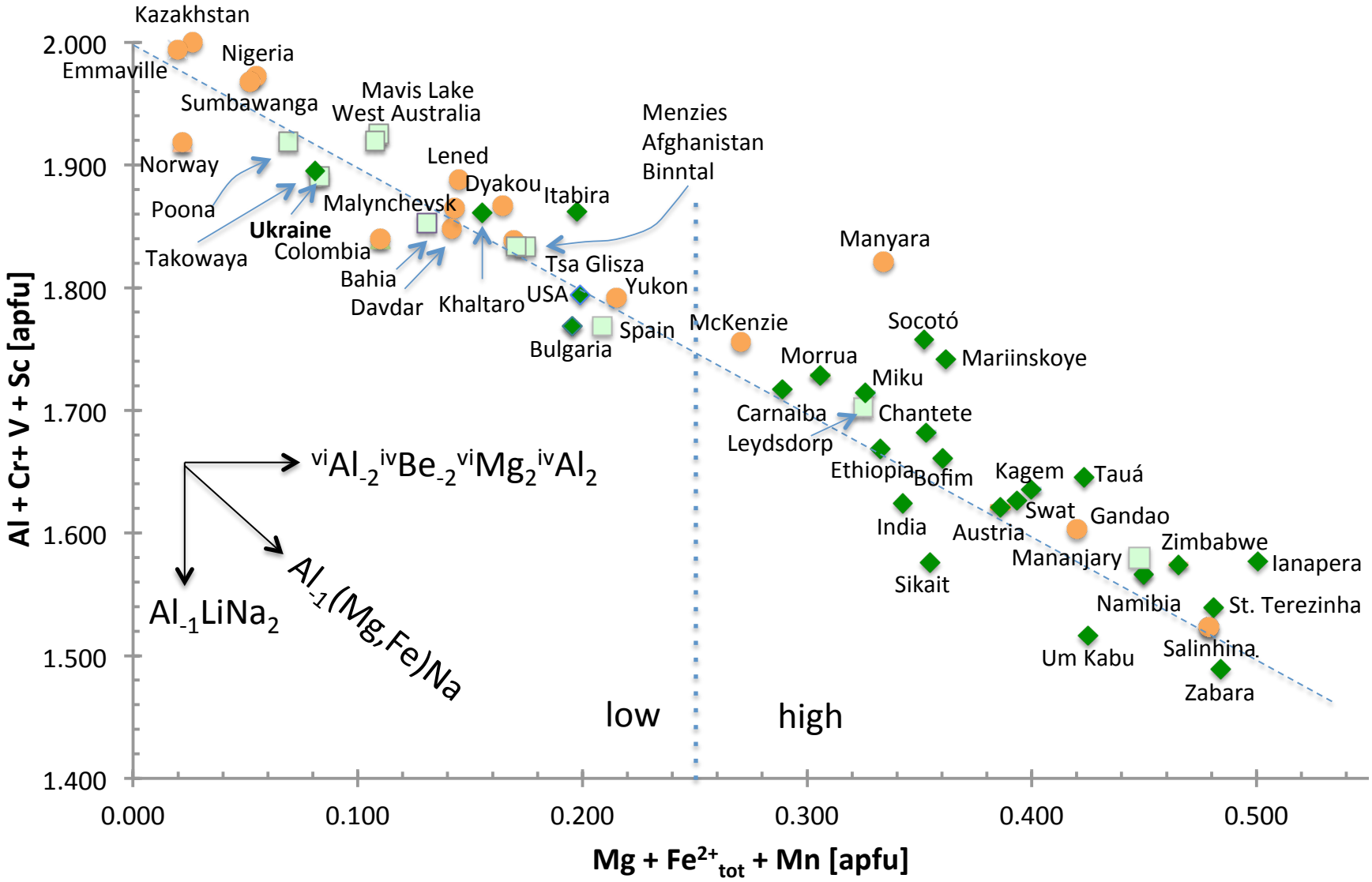
Kazakhstan
Nigeria
Emmaville
Sumbawanga
Mavis Lake
West Australia
Menzies
Afghanistan
Binntal
Lened
Norway
Dyakou
Itabira
Poona
Malynchevsk
Ukraine
Takowaya
Colombia
Tsa Glisza
Bahia
Yukon
Davdar
Khaltaro
USA
Spain
Bulgaria
Manyara
McKenzie
Socotó
Morrua
Mariinskoye
Miku
Carnaiba
Chantete
Leydsdorp
Ethiopia
Bofim
Kagem
Tauá
Swat
Gandao
India
Austria
Zimbabwe
Mananjary
Ianapera
Sikait
Namibia
St. Terezinha
Salinhina
Um Kabu
Zabara
low
high
$^{vi}Al_{-2}{}^{iv}Be_{-2}{}^{vi}Mg_2{}^{iv}Al_2$
$Al_{-1}LiNa_2$
$Al_{-1}(Mg,Fe)Na$
2.000
1.900
1.800
1.700
1.600
1.500
1.400
0.000
0.100
0.200
0.300
0.400
0.500
Al + Cr+ V + Sc [apfu]
Mg + Fe^{2+}_{tot} + Mn [apfu]

Fig. 14

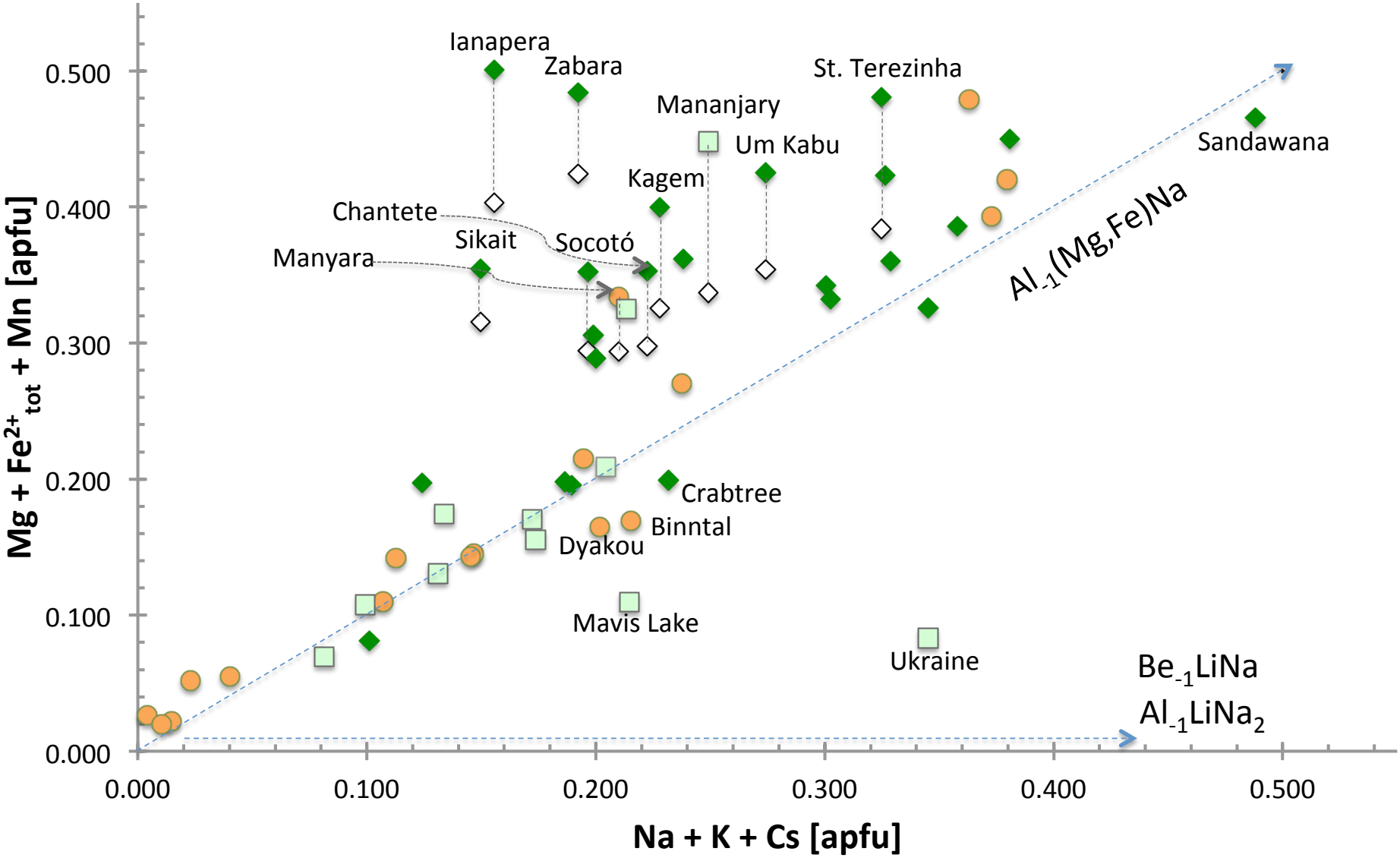
Ianapera
Zabara
St. Terezinha
Mananjary
Um Kabu
Sandawana
Kagem
Chantete
Sikait
Socotó
Manyara
Al-1(Mg,Fe)Na
Crabtree
Binntal
Dyakou
Mavis Lake
Ukraine
Be-1LiNa
Al-1LiNa2
0.500
0.400
0.300
0.200
0.100
0.000
0.000
0.100
0.200
0.300
0.400
0.500
Mg + Fe2+tot + Mn [apfu]
Na + K + Cs [apfu]

Fig. 15